

Copyright © 1981, by the author(s).
All rights reserved.

Permission to make digital or hard copies of all or part of this work for personal or classroom use is granted without fee provided that copies are not made or distributed for profit or commercial advantage and that copies bear this notice and the full citation on the first page. To copy otherwise, to republish, to post on servers or to redistribute to lists, requires prior specific permission.

KINK INSTABILITIES IN LONG ION LAYERS

by

Douglas S. Harned

Memorandum No. UCB/ERL M81/73

16 September 1981

ELECTRONICS RESEARCH LABORATORY

College of Engineering
University of California, Berkeley
94720

Kink Instabilities in Long Ion Layers

Douglas S. Harned

Electronics Research Laboratory

University of California

Berkeley, CA 94720

ABSTRACT

Kink instabilities in long ion layers immersed in a dense background plasma are studied. A numerical extension of the analytic model of Lovelace indicates that these instabilities will occur for values of the self-magnetic field index below those predicted previously. A quasineutral hybrid simulation code has been used to verify these lower thresholds. The simulations also show that the end of exponential growth occurs due to a nonlinear shift in the betatron frequency at large amplitude, producing an increase in layer thickness and a layer which has many non-axis-encircling ions.

I. INTRODUCTION

Field-reversing ion layers have been considered as a possible means of confining and heating a fusion plasma. It has also been proposed that such ion layers could provide a stabilizing influence on the tilt mode in the spheromak^{1,2}. However, ion layers may be unstable due to a kink mode which results from the coupling of compressional Alfvén waves with the betatron motion of the layer particles.

The ion layer configuration is shown in Fig. 1. An ion beam, at radius R and of thickness a , flows perpendicularly to an external magnetic field, $\vec{B}_e = B_z^e \hat{z}$. The beam current, $J_{b\theta}$, produces a self-magnetic field, B_z^s , which may be large enough to reverse the total magnetic field on axis. The layer is immersed in a background plasma such that $n_b \ll n_p$, where n_b and n_p are the densities of the beam and plasma, respectively. The background plasma is assumed to be sufficiently dense that $v_A^2 \ll \bar{v}_\theta^2$, where v_A is the background plasma Alfvén speed, $v_A \equiv B_z^e / (4\pi n_p M_p)^{1/2}$, and \bar{v}_θ is the average rotational velocity of the beam. M_p is defined to be the mass of an ion in the background plasma. A conducting wall is located at radius $r = r_w$. There is no variation in the axial direction ($\partial/\partial z = 0$). It is this case, $k_z = 0$, which is expected to be the most unstable for a long layer. This has been indicated by Sudan and Rosenbluth³ through the application of an energy principle derived from the Vlasov equation to obtain sufficient conditions for stability. Kink modes in these layers correspond to perturbations of the form $\vec{\epsilon} = \hat{r} \epsilon_r \exp(im\theta - i\omega t)$ with $m \geq 2$. This paper discusses the results of theory and simulations concerning the linear and nonlinear behavior of these modes. The term "kink", in reference to these modes, arises because the azimuthal mode number, m , is analogous to the toroidal mode number of a thin ring, or "bicycle tire", configuration.

Section II presents theoretical results for instability thresholds and linear growth rates as determined by a numerical generalization of an analysis by Lovelace⁴. Section III describes the model for our hybrid simulation code which has been used to study ion layer kink modes. The simulation results pertaining to the linear behavior of kink instabilities are presented in Sec. IV. Comparisons are made with the results of Sec. II. Section V describes the nonlinear behavior of kink modes as observed in the hybrid simulations.

II. LINEAR THEORY

The linear stability of kink modes has been studied by Lovelace in the approximation of a linear beam^{5,6} and as a long layer⁴, neglecting axial variation. Similar instabilities have been studied by Finn and Sudan⁷ in the bicycle tire limit. Our model follows that of Lovelace⁴ in which kink and precessional modes, corresponding to perturbations in radius of the form $\bar{\epsilon} = \hat{r}\epsilon_r \exp(im\theta - i\omega t)$, were studied. In this paper we consider the case in which the external magnetic field is uniform. In this case the precessional mode ($m=1$) is neutrally stable. We will restrict this analysis to modes with $m \geq 2$ (i.e., kink modes).

The analysis of Lovelace⁴ treated the background plasma ions and electrons as fluids. The layer was assumed to be composed of collisionless ions with their behavior described by the particle equations of motion. The layer was assumed to be thin, $(a/R)^2 \ll 1$, and the modes were assumed to be of low frequency, such that $(\omega/\Omega)^2 \ll 1$, where Ω is the layer rotation frequency. This assumption allows the forces on the layer particles to be given by averages over the layer thickness. The perturbation, ϵ_r , was assumed to be first order, $(\epsilon_r/a) \ll 1$, as were the perturbed field

quantities, $\delta B_z/B_z \ll 1$, $\delta E_r/E_r \ll 1$, and $\delta E_\theta/E_\theta \ll 1$. The equations were linearized; i.e., second and higher order terms were neglected. The following equations were obtained by Lovelace⁴ for the perturbation ϵ_r :

$$(d^2/dt^2)\epsilon_r = -\Omega^2(1+\eta_s)\epsilon_r + \delta F_r \quad (1a)$$

$$\delta F_r \equiv \frac{q\bar{v}_\theta}{M_b c} \langle \delta B_z \rangle + \frac{q}{M_b} \langle \delta E_r \rangle - \frac{iq}{M_b m} \langle \delta E_\theta \rangle \quad (1b)$$

$$\eta_s \equiv -\frac{q\bar{v}_\theta}{M_b c \Omega^2} \left\langle \frac{\partial}{\partial r} B_z^s \right\rangle \quad (1c)$$

where the radial averages are weighted by the beam current,

$$\langle (...) \rangle \equiv \int r dr J_b(r) (...) / \int r dr J_b(r).$$

M_b is defined to be the mass of a layer ion, \bar{v}_θ the average layer rotation velocity, and η_s is the self-magnetic field index, which is approximately equal to $(\omega_\beta/\Omega)^2$. The layer betatron frequency, ω_β , is the average frequency at which the ions oscillate radially in the self-magnetic field of the layer. Defining ζ to be the field-reversal factor,

$$\zeta \equiv \left| (B_z^s(r=0)) / B_z^e \right|,$$

makes η_s of order $(2R/a)\zeta$. (Note that this definition of ζ is not the same as used by Lovelace⁴). The perturbed field quantities are determined by the following equations⁴:

$$\left(\frac{i\omega}{c} \right) \delta E_r = -\Lambda_a \frac{im}{r} (\Delta B_z + \phi) - \Lambda_b \left(\frac{\partial}{\partial r} \Delta B_z + \frac{\phi}{r} \right) \quad (2a)$$

$$\left(\frac{i\omega}{c} \right) \delta E_\theta = -\Lambda_b \frac{im}{r} (\Delta B_z + \phi) + \Lambda_a \left(\frac{\partial}{\partial r} \Delta B_z + \frac{\phi}{r} \right) \quad (2b)$$

where

$$\Lambda_a \equiv \left(\frac{v_A}{c} \right)^2 \frac{1 + (v_A/c)^2}{(1 + (v_A/c)^2)^2 - (\omega/\omega_{ci})^2} \quad (2c)$$

$$\Lambda_b \equiv \left(\frac{v_A}{c} \right)^2 \frac{i\omega}{(1 + (v_A/c)^2)^2 - (\omega/\omega_{ci})^2} \quad (2d)$$

$$\Delta B_z \equiv \delta B_z - (4\pi/c) \epsilon_r J_b \quad (2e)$$

$$\phi \equiv (\omega r / m\bar{v}_\theta) 4\pi\epsilon_r J_b / c. \quad (2f)$$

ΔB_z is obtained from solving the differential equation

$$\begin{aligned} \frac{1}{r} \frac{\partial}{\partial r} \left(r \Lambda_a \frac{\partial}{\partial r} \Delta B_z \right) + \left(\frac{\omega^2}{c^2} - \frac{m^2 \Lambda_a}{r^2} \right) \Delta B_z - \frac{im}{r} \left(\frac{\partial}{\partial r} \Lambda_b \right) \Delta B_z \\ = \left(\frac{m^2 \Lambda_a}{r^2} - \frac{\omega m \bar{v}_\theta}{c^2 r} \right) \phi - \frac{1}{r} \frac{\partial}{\partial r} (\Lambda_a \phi) + \frac{\partial}{\partial r} \left(\frac{im \Lambda_b \phi}{r} \right). \end{aligned} \quad (3)$$

Assuming that J_b and E_θ vanish at a conducting wall at $r=r_w$, Eq. 2b provides the boundary condition on ΔB_z :

$$\left(\frac{1}{\Delta B_z} \frac{\partial}{\partial r} \Delta B_z \right)_{r=r_w} = \frac{im \Lambda_b(r_w)}{r_w \Lambda_a(r_w)}. \quad (4)$$

Note that Λ_b and Λ_a are functions of radius because they depend on v_A which, in a strong ion layer, will normally depend on r .

Lovelace⁴ used Eqs. 1,2,3, and 4 to solve for the instability thresholds and growth rates. In order to do this analytically, it was assumed that $v_A^2 \approx \text{constant}$ and that the layer had sharp boundaries. Thresholds were obtained for two cases: (1) $\omega^2 \ll (v_A/a)^2$ and (2) $\omega^2 < (v_A/a)^2$ with $\omega_r^2 \ll \gamma^2$, where ω_r and γ are the real and imaginary parts of the frequency. In both cases $\eta_s < m^2 - 1$ was found to be sufficient for stability. The assumption $v_A^2 \approx \text{constant}$ implies that the plasma density is smaller inside than outside the layer. This assumption does not correspond to the situation in real three-dimensional systems when the field-reversal factor is close to or greater than unity. This is because in real systems the density will not have large variations along a given closed field line. The comment is made by Lovelace⁴ that it appears feasible to solve Eq. 3 numerically in order to remove this difficulty.

We have chosen to extend the analysis of Lovelace⁴ in order to eliminate the assumption of constant Alfvén speed, as well as the frequency restrictions $\omega^2 < (v_A/a)^2$

and $\omega_r^2 < \gamma^2$, by performing a numerical solution of the system of Eqs. 1, 2, 3, and 4. The procedure used for this numerical solution is described in Appendix A.1. Rather than a sharp boundary layer equilibrium distribution, an exponential rigid rotor equilibrium⁸ is treated. The beam current density for this distribution is

$$J_{b\theta}(r) = en_0\Omega r \operatorname{sech}^2\left(\frac{r^2 - r_1^2}{r_0^2}\right) \quad (5)$$

and the magnetic field profile is

$$B_z(r) = \frac{-2M_b v_i^2 c}{e\Omega r_0^2} \tanh\left(\frac{r^2 - r_1^2}{r_0^2}\right) \quad (6)$$

In Eqs. 5 and 6, v_i is the thermal velocity of the rigid rotor distribution, r_1 and r_0 are adjustable parameters, and n_0 is a normalization factor for the density. The equilibrium background plasma density is considered to be uniform.

Our numerical results show significant differences from the analytic results of Lovelace⁴. In particular we find the instability threshold for a given mode to occur at somewhat lower values of η_s than $m^2 - 1$. Additionally, we have found that the instability thresholds are influenced by the Alfvén transit time across the layer thickness. The approximate thresholds are summarized in Table 1 for different values of the Alfvén transit time. One can see from Table 1 that for a fixed layer thickness, a , an increased background density provides a stabilizing effect. The mode with the lowest instability threshold in η_s is the $m=2$ mode. The low thresholds here imply that a thick layer, $a \approx R$, is a necessary condition for an ion layer to be stable near field-reversal ($\zeta \approx 1$) (this condition can only be called a necessary one since this analysis requires $a \ll r$ to determine a growth rate). These results were not available under the simplifying assumptions used by Lovelace⁴ because near the thresholds $\omega_r > \gamma$ and $\omega \approx v_A/a$.

The real and imaginary parts of the frequency of modes for a layer with $(R/a)=5$ are shown as a function of field-reversal factor, ζ , in Figs. 2 and 3. The maximum growth rate for a given mode occurs when $\omega_r^2 \approx (\omega_\beta - m\Omega)^2$. Lovelace⁴ found the growth rates to be linearly proportional to the Alfvén speed. We find that the critical factor is not simply the Alfvén speed, but the Alfvén transit time across the layer thickness. The growth rate of the $m=2$ mode for layers of varying background density are shown in Fig. 4 for a layer with $R/a \approx 5$. As the Alfvén transit time becomes very large and $\omega^2 \gg v_A^2/a^2$, then the mode will be stabilized because the layer will no longer behave rigidly.

For cases in which the assumptions of Lovelace⁴ are valid, our growth rates reduce to those obtained analytically.

III. SIMULATION MODEL

The simulation code that we have used to study ion layer kink instabilities is a two-dimensional, fully nonlinear, quasineutral hybrid code. Such codes have been used in one-dimensional problems by Byers et al.⁹ and in two-dimensional studies of theta pinch implosions by Hewett¹⁰. Because ion layers are characterized by ion Larmor radii comparable to the system size, it is necessary to treat the ions as particles. Since the time scales of kink modes are much longer than the ion-cyclotron period, it is unnecessary to follow the details of the electron dynamics. Hence, the electrons are considered to be an inertialess fluid. In addition, electromagnetic radiation effects are not important on these time scales, allowing us to use the Darwin version of Ampere's law (i.e., the transverse displacement current is neglected).

The Darwin version of Ampere's law is combined with the inertialess version of

the electron momentum equation and the assumption of quasineutrality to determine the electric field. The expression for the electric field (as derived in Ref. 11, or similarly in Ref. 9) is

$$\bar{E} = \frac{1}{4\pi n_i e} (\nabla \times \bar{B}) \times \bar{B} - \frac{1}{n_i e c} \bar{J}_i \times \bar{B} - \frac{1}{n_i e} \nabla (n_i T_e). \quad (7)$$

In Eq. 7 the ion density, n_i , and ion current density, \bar{J}_i , are determined from the ion particles by linear weighting (particle-in-cell) from the grid. The magnetic field is advanced in time by Faraday's law and the ions are moved by the equations of motion. A more detailed description of this code may be found in Ref. 11.

The equations are solved in the $r-\theta$ plane (see Fig. 1). However, for numerical reasons, cartesian coordinates are used in the simulation. No axial variation is allowed (i.e., $\partial/\partial z=0$) and B_x , B_y , E_z , J_z , and v_z are all set equal to zero. Doubly periodic boundaries have been used in the simulation results discussed here. A conducting wall at radius r_w has a weakly stabilizing effect on ion layer kink modes. The results of Lovelace⁴ indicate that the effect of the wall will be negligible unless $(r_w - R)/R \ll 1$; we have confirmed this result by the numerical calculations described in Sec. II.

Our simulations begin with the loading of a cold uniform background plasma of fluid electrons and particle ions with a uniform density n_p . Then a Vlasov equilibrium (i.e., $\partial f/\partial t=0$) ion layer distribution, corresponding to an exponential rigid rotor,

$$f(r, v_r, v_\theta) = \frac{n_0}{\pi v_i^2} \operatorname{sech}^2 \left(\frac{r^2 - r_1^2}{r_0^2} \right) \exp \left\{ - \frac{[v_r^2 + (v_\theta - r\Omega)^2]}{v_i^2} \right\}, \quad (8)$$

is added. This distribution produces the ion current and magnetic field profiles described in Sec. II. Fluid electrons are present in the layer, in the same initial profile, to provide charge neutralization. However, all current is initially carried by the ions.

The ion layer is assumed to be tenuous relative to the background plasma, so that $n_b \ll n_p$ and $v_A^2 \ll \bar{v}_\theta^2$, as in Sec. II. The layer ions are represented by 40,000 particles. 40,000 particles are also used to represent the background plasma ions. Finite differencing is performed on a 100 by 100 grid and the time step is $\omega_{ci} \Delta t = 0.1$.

IV. SIMULATION RESULTS: LINEAR BEHAVIOR

Simulations have been performed using the code described in Sec. III to study the linear and nonlinear behavior of ion layer kink instabilities. Figure 5 shows the initial particle positions for an exponential rigid rotor ion layer; the background plasma is also represented by particles, but these are not shown on this plot. The field-reversal factor for this case is $\zeta = 1.1$ (B_z slightly reversed on axis). The rigid rotor distribution of Eq. 6 has parameters set to $r_1 = 2.5$ and $r_0 = 1.35$, corresponding to $R/a \approx 6$. The self-magnetic field index for this case is $\eta_s = 5.9$ and the normalized inverse Alfvén transit time is $v_A/\omega_{ci} a \approx 0.1$. Table 1 indicates that this Vlasov equilibrium should be unstable to both the $m=2$ and $m=3$ modes. Figure 6 shows the layer at time $t = 50\omega_{ci}^{-1}$, when an $m=3$ mode has grown to large amplitude. The $m=3$ character is clearly evident in Fig. 7, which shows the azimuthal electric field contours. At a later time, $t = 100\omega_{ci}^{-1}$, an $m=2$ mode clearly dominates, as can be seen in Figs. 8 and 9. At a much later time, $t = 300\omega_{ci}^{-1}$, the layer has become very thick and the earlier mode structure has disappeared, as seen in Fig. 10.

The numerical calculation described in Sec. II predicts the linear growth rate for the $m=2$ mode to be $\gamma/\omega_{ci} = 0.065$, and for the $m=3$ mode to be $\gamma/\omega_{ci} = 0.112$. Growth rates were obtained from the simulation by measuring the perturbation in the average radial particle position as a function of angle, $\delta r(\theta, t) = (\langle r(\theta, t) \rangle - R)$. $\delta r(\theta)$

is then decomposed into its Fourier components. $(\delta r(t))^2$ for the $m=2$ and $m=3$ modes is shown in Figs. 11 and 12. The growth rate for the $m=2$ mode is found to be $\gamma/\omega_{ci}=0.065$, and the growth rate for the $m=3$ mode is found to be $\gamma/\omega_{ci}=0.101$, very close to the expected values. The $m=1$ mode and modes with $m \geq 4$ were found to be stable, as predicted. In Fig. 2 the growth rates measured from simulations are plotted as a function of field-reversal factor, with the results from Sec. II for modes $m=2, 3, 4$, and 5. Figure 4 shows the results of simulation and theory, giving growth rates as a function of the inverse Alfvén transit time. In both cases we find good agreement for linear growth rates. The simulations have also confirmed the predictions that the instability thresholds should be lower in terms of η_s than the previous analytic results⁴.

In order to obtain the azimuthal mode components of $(\delta r)^2$ (shown in Figs. 11 and 12) used to determine the growth rates, the values of $\delta r(\theta)$ from $\theta=0$ to $\theta=2\pi$ were used. Because this information always contains an integer number of wavelengths for an unstable mode, the real frequency of oscillation cannot be obtained from the growth rate diagnostics. Real frequencies were determined by measuring the frequency of the radial perturbation at a fixed angle. Because the real frequency of these modes is comparable to the growth rate, $(\delta r)^2$ may grow several decades in one period of oscillation. This made the measurement of real frequencies difficult except for cases in which one mode dominated for a long period of time. For the limited number of cases in which real frequencies could be evaluated, they were found to agree with the predictions of Sec. II to within ten percent.

The physical mechanism for ion layer kink instabilities is the resonant interaction of the betatron motion of layer particles with compressional Alfvén waves in the background plasma, which occurs when $\omega \approx \omega_\beta - m\Omega$. The maximum growth rates are

expected to occur when the largest number of particles are experiencing resonant betatron motion. This should occur when $\omega_\beta \approx m\Omega$, since $\omega^2 \ll \Omega^2$. This has been observed in both our simulations and in the numerical calculations described in Sec. II, as the peaks in Fig. 2 correspond to points where $\omega_\beta \approx m\Omega$. The growth of the $m=3$ mode in the preceding example may be traced to the fact that most particles in this layer have betatron motion characterized by $\omega_\beta/\Omega=3$. An example of a particle orbit from $t=0$ to $t=60\omega_{ci}^{-1}$ is shown in Fig. 13, with the $m=3$ character clearly present. One reason that thresholds may occur at lower values of the self-magnetic field index than $\eta_s = m^2 - 1$ is because even when the mean betatron frequency of the layer is too small to produce a resonant interaction, the thermal spread of the layer ions can still allow a substantial number of particles to resonate at a higher betatron frequency and drive the instability.

V. SIMULATION RESULTS: NONLINEAR BEHAVIOR

Nonlinear effects which halt the growth of ion layer kink instabilities have been identified. Figures 11 and 12 show the end of exponential growth, or saturation of the $m=2$ and $m=3$ instabilities for the unstable configuration of Sec. IV. The common observation at saturation has been a nonlinear shift in the layer betatron frequency which diminishes the resonant interaction of layer particles required to produce kink instabilities.

During the growth of kink instabilities, a large fraction of the directed beam energy is lost to thermal energy. This can be seen in Figs. 14 and 15, which show the directed and thermal energies of the layer as a function of time. The thermal layer pressure increases and is no longer in equilibrium with the magnetic forces compress-

ing the layer. This pressure imbalance causes the layer to expand. The change in layer thickness is clearly visible in Figs. 6 and 8, after the $m=2$ and $m=3$ instabilities have grown to large amplitude. A measure of the expansion with time is shown in Fig. 16, which plots $\langle (r - \langle r(\theta) \rangle)^2 \rangle$ as a function of time. The significant point is that the layer betatron frequency is roughly proportional to R/a . Therefore, as the layer increases its thickness, a , the betatron frequency and consequently the self-magnetic field index is reduced. When the layer becomes sufficiently thick so that the self-magnetic field index drops below the instability threshold for a given mode, that mode ceases to grow exponentially, although nonlinear effects, producing layer heating, have been observed to persist somewhat beyond that point. An additional factor is that the layer expansion increases the Alfvén transit time across the layer, which tends to stabilize the instability. This effect, however, is small compared to that produced by the shift in betatron frequency.

The effects of the nonlinear shift in betatron frequency can be seen in the example of Sec. IV. The $m=3$ mode has the largest growth rate and is the dominant mode at early times. However, at $t=56\omega_{ci}^{-1}$ the $m=3$ mode stops growing. At this point the self-magnetic field index is $\eta_s=4.35$ with $v_A/a\omega_{ci}=0.074$. It can be seen from Table 1 that these values are very close to the linear threshold of the $m=3$ mode. The $m=2$ mode is still linearly unstable and continues to grow until it eventually exceeds the amplitude of the saturated $m=3$ mode, and then becomes the dominant mode, as seen in Fig. 8. At $t=114\omega_{ci}^{-1}$ the $m=2$ mode stops growing. At this point $\eta_s=2.11$ and $v_A/a\omega_{ci}=0.036$. The Table 1 values can only be expected to give an approximate result for this mode, since the layer has become thick enough so that the self-magnetic field index is only an approximate concept as defined by Eq. 1c. Neverthe-

less, the $m=2$ mode stops growing at a time when η_s is very near the threshold predicted by Table 1. Similar cascades have been observed for higher azimuthal mode numbers. For higher azimuthal mode numbers the mode with the largest mode number will saturate first, followed by the successive saturation of the lower mode numbers beginning with the largest remaining unstable mode and ending with the saturation of the $m=2$ mode. It is rarely possible, however, to see clearly more than two modes because the layer expands rapidly enough that the betatron frequency will drop below the thresholds of modes before they can grow to a sufficiently large amplitude to dominate. Nevertheless, the final state is similar, regardless of the number of unstable modes present in the initial equilibrium. This has been confirmed in simulations of thinner layers, which have had modes up to $m=5$ unstable, yet result in virtually the same final state as the previously discussed example.

After all of the initial instabilities have saturated, the resultant thick layer appears to be stable. No further instabilities have been observed for times as long as $t=500\omega_{ci}^{-1}$. However, the final state has a very high noise level and we cannot exclude the possibility that instabilities may exist with smaller growth rates than those of the initial kink modes. The layer is characterized by being thick, but still field-reversed. This can be seen by the initial and final magnetic field profiles shown in Fig. 17. For stronger layers, with field-reversal factors as large as $\zeta=1.8$, the observed behavior has been qualitatively the same, in that the final state is much thicker, relatively stable, and field-reversal is maintained. The instabilities do not result in the loss of the layer, but the final state has substantial electron currents and many non-axis-encircling ions. The nature of the change in orbits can be seen in Fig. 18. The large axis-encircling part of the orbit (see Fig. 13) corresponds to the initial $m=3$ betatron motion, which

drives the initial instability. As the layer broadens, the motion changes to $m=2$ betatron motion and finally the orbit becomes non-axis-encircling when the layer thickness becomes comparable to its major radius.

As a check on numerical accuracy, total energy has been monitored and has been found to be conserved to within two percent of the variation of potential and kinetic energies. Additional results of ion layer kink instability simulations are presented in Appendix A.2.

VI. SUMMARY

The analysis of Lovelace⁴ has been generalized numerically. The numerical results show that the thresholds are at lower values of the self-magnetic field index than predicted by earlier analytic results. Simulations have confirmed these lower values of the instability thresholds. Instabilities have been found to grow on magnetohydrodynamic time scales; i.e. $\gamma \approx v_A/a$. Nonlinear effects have been found to reduce the betatron frequency of the layer so that ion betatron motion is no longer resonant with the wave, halting exponential instability growth.

Although this study is only two-dimensional, the same type of behavior might be expected for the fully three-dimensional case, since Finn and Sudan⁷ have obtained similar results for the linear stability of ion layers in the bicycle tire limit. It is possible that the kink instability could be stabilized by the addition of a toroidal component of the magnetic field¹². Without a toroidal field it appears that the use of ion layers, carrying a substantial part of the current needed to produce field-reversal, is possible only for thick layers with large numbers of non-axis-encircling particles.

ACKNOWLEDGMENTS

The author is indebted to Prof. C.K. Birdsall for his discussions, advice, and encouragement during the course of this work. Many valuable discussions were also held with Drs. A. Friedman and B.I. Cohen.

This work was supported by ONR Contract No. N00014-17-C0578. Computations were performed at the National Magnetic Fusion Energy Computer Center at Livermore.

REFERENCES

1. R.N. Sudan and P. Kaw, "Stabilizing Effect of High Energy Axis-Encircling Particles on the Tilting Instability of Spheromak-Type Equilibria", *Bull. Am. Phys. Soc.* **25**, p. 970 (1980).
2. H.H. Fleischmann, "On the Use of Intense Electron and Ion Beams and Rings in Mixed-CT Configurations", *Proceedings of the Third Symposium on the Physics and Technology of Compact Toroids in the Magnetic Fusion Energy Program*, (Los Alamos, 1980).
3. R.N. Sudan and M.N. Rosenbluth, "Stability of Axisymmetric Field-Reversed Equilibria of Arbitrary Ion Gyroradius", *Phys. Fluids* **22**, pp. 282-293 (1979).
4. R.V. Lovelace, "Precession and Kink Motion of Long Astron Layers", *Phys. Fluids* **22**, pp. 708-717 (1979).
5. R.V. Lovelace, "Low Frequency Stability of Astron Configurations", *Phys. Rev. Lett.* **35**, pp. 162-164 (1975).
6. R.V. Lovelace, "Astron Kink Stability with a Toroidal Magnetic Field", *Phys. Rev. Lett.* **41**, pp. 1801-1804 (1978).
7. J.M. Finn and R.N. Sudan, "Betatron Resonance Instabilities in Axisymmetric Field-Reversed Systems", *Phys. Fluids* **22**, pp. 1148-1153 (1979).
8. R.C. Davidson, *Theory of Nonneutral Plasmas*, W.A. Benjamin Inc. (London, 1974).
9. J.A. Byers, B.I. Cohen, W.C. Condit, and J.D. Hanson, "Hybrid Simulation of Quasineutral Phenomena in Magnetized Plasma", *J. Comput. Phys.* **27**, pp. 363-396 (1978).

10. D.W. Hewett, "A Global Method of Solving the Electron-Field Equations in a Zero-Inertia-Electron-Hybrid Plasma Simulation Code", *J. Comput. Phys.* **38**, pp. 378-395 (1980).
11. D.S. Harned, "Quasineutral Hybrid Simulation of Macroscopic Plasma Phenomena", in preparation for submittal to *J. Comput. Phys.*
12. J.M. Finn, "Kink Instabilities of a Field-Reversed Ion Ring with a Toroidal Magnetic Field", *Phys. Fluids* **22**, pp. 1770-1781 (1979).

Instability Thresholds				
$v_A/\omega_{ci}a$	η_s			
	$m=2$	$m=3$	$m=4$	$m=5$
.20	0.4	2.2	5.0	8.5
.10	1.0	4.2	8.0	12.0
.05	1.8	5.0	9.5	15.0
.025	2.0	6.0	11.0	18.0
m^2-1	3.0	8.0	15.0	24.0

TABLE 1. Approximate ion layer kink instability threshold values of the self-magnetic field index, η_s , at different values of $(v_A/\omega_{ci}a)$. The thresholds were determined by the numerical calculations discussed in Sec. II. The threshold values of η_s as determined analytically by Lovelace, $\eta_s = m^2 - 1$, are also given.

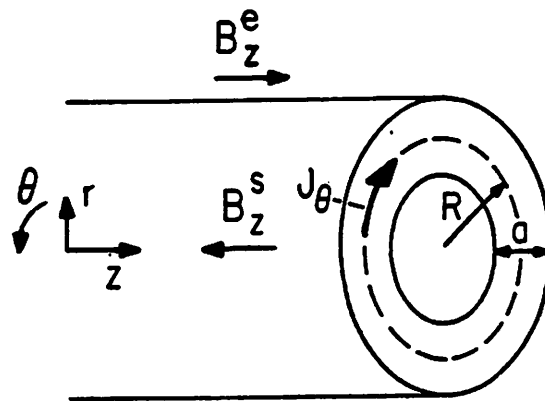


FIG. 1. The ion layer configuration. J_θ is in $-\theta$ direction.

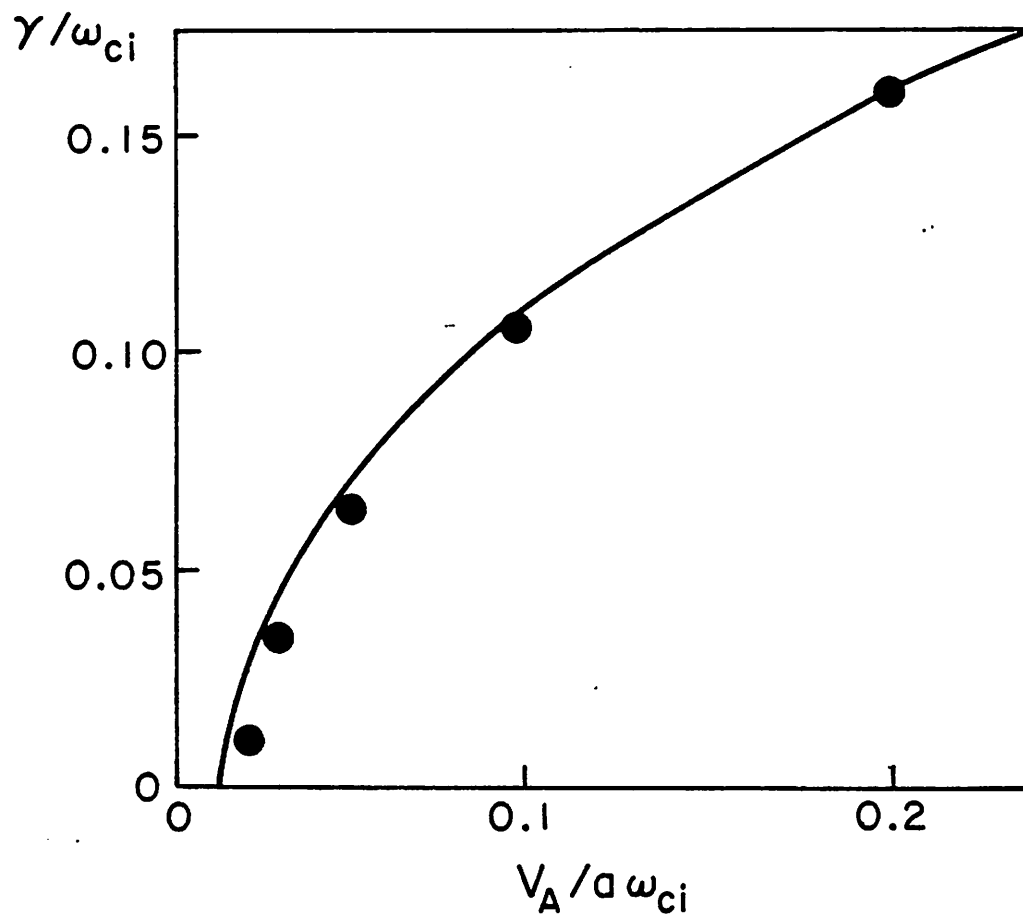


FIG. 4. Linear growth rates, γ , for the $m=2$ mode as a function of the inverse Alfvén transit time. The solid curve represents the numerical solution of Sec. II and the points are the results of hybrid simulations. $R/a=5$ and $\zeta=0.65$.

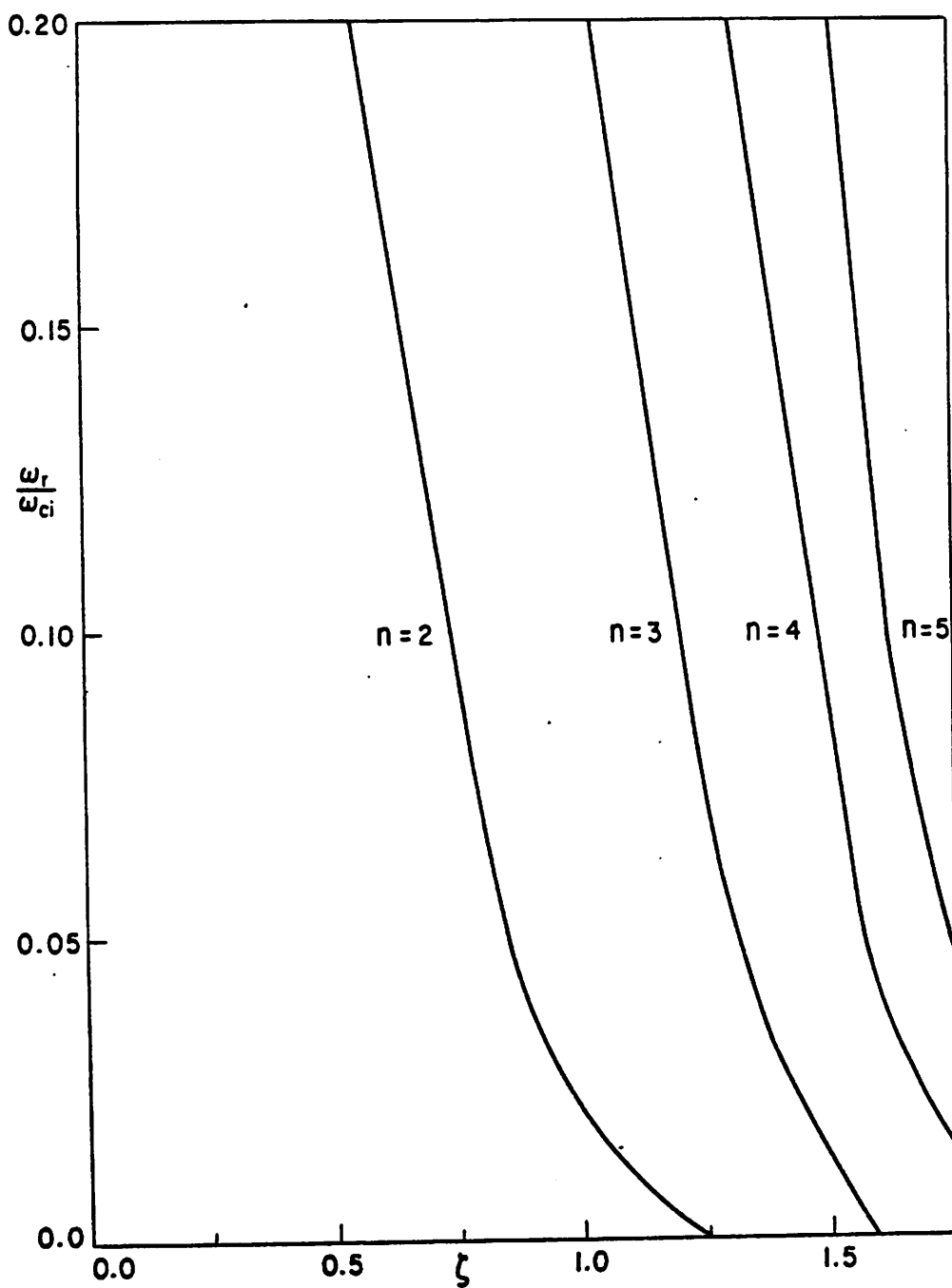


FIG. 3. Real frequencies, ω_r , as a function of field-reversal factor, ζ , as determined by the numerical solution of Sec. II. $R/a=5$ and $\nu_A/(\omega_{ci}a)=0.1$.

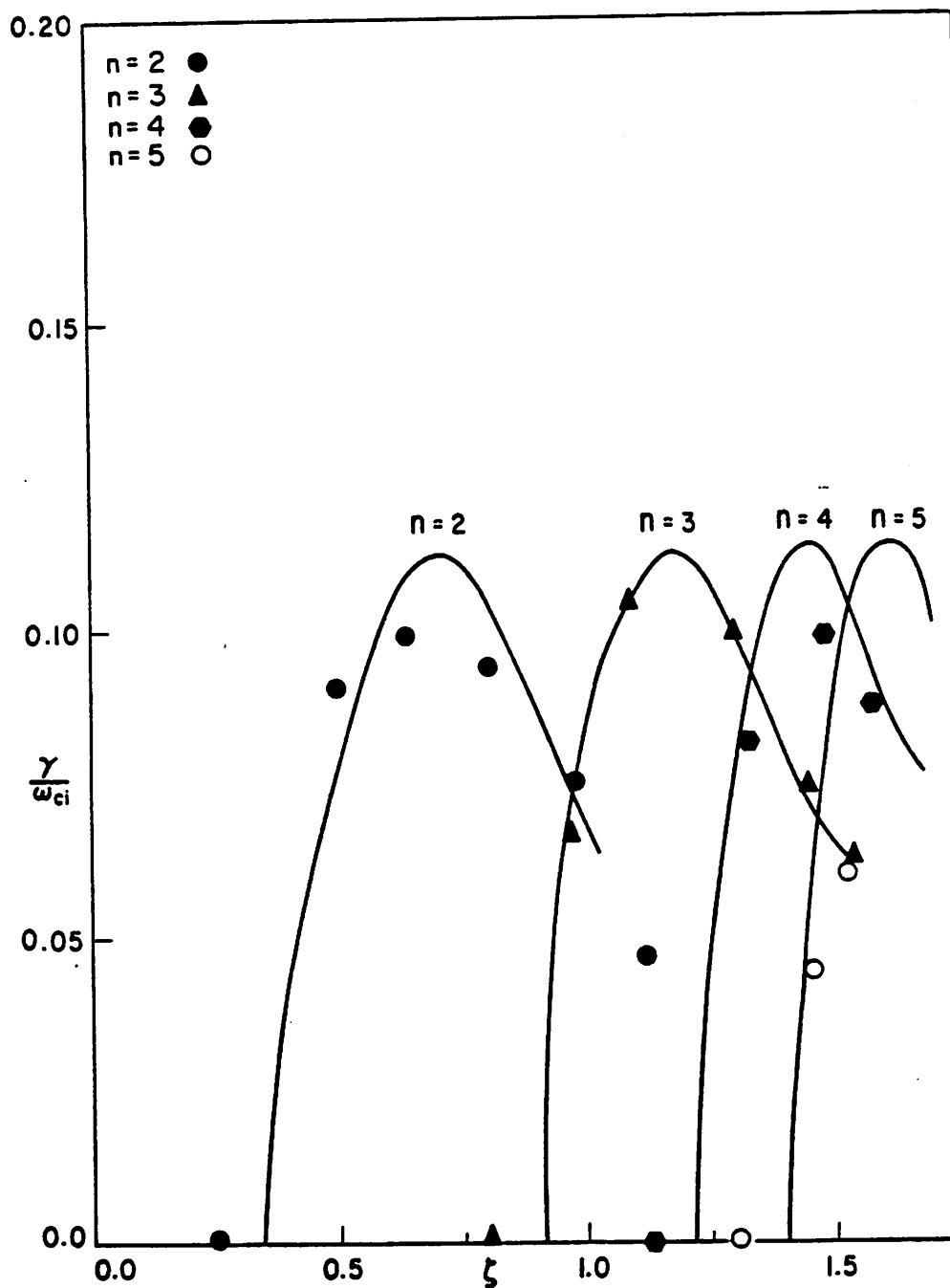


FIG. 2. Linear growth rates, γ , for ion layer kink instabilities as a function of field-reversal factor, $\zeta \equiv |B_z^i(r=0)/B_z^e|$. The solid curves are the results of the numerical solution of Sec. II. The points are the results of hybrid simulations. $R/a=5$ and $v_A/(a\omega_{ci})=0.1$.

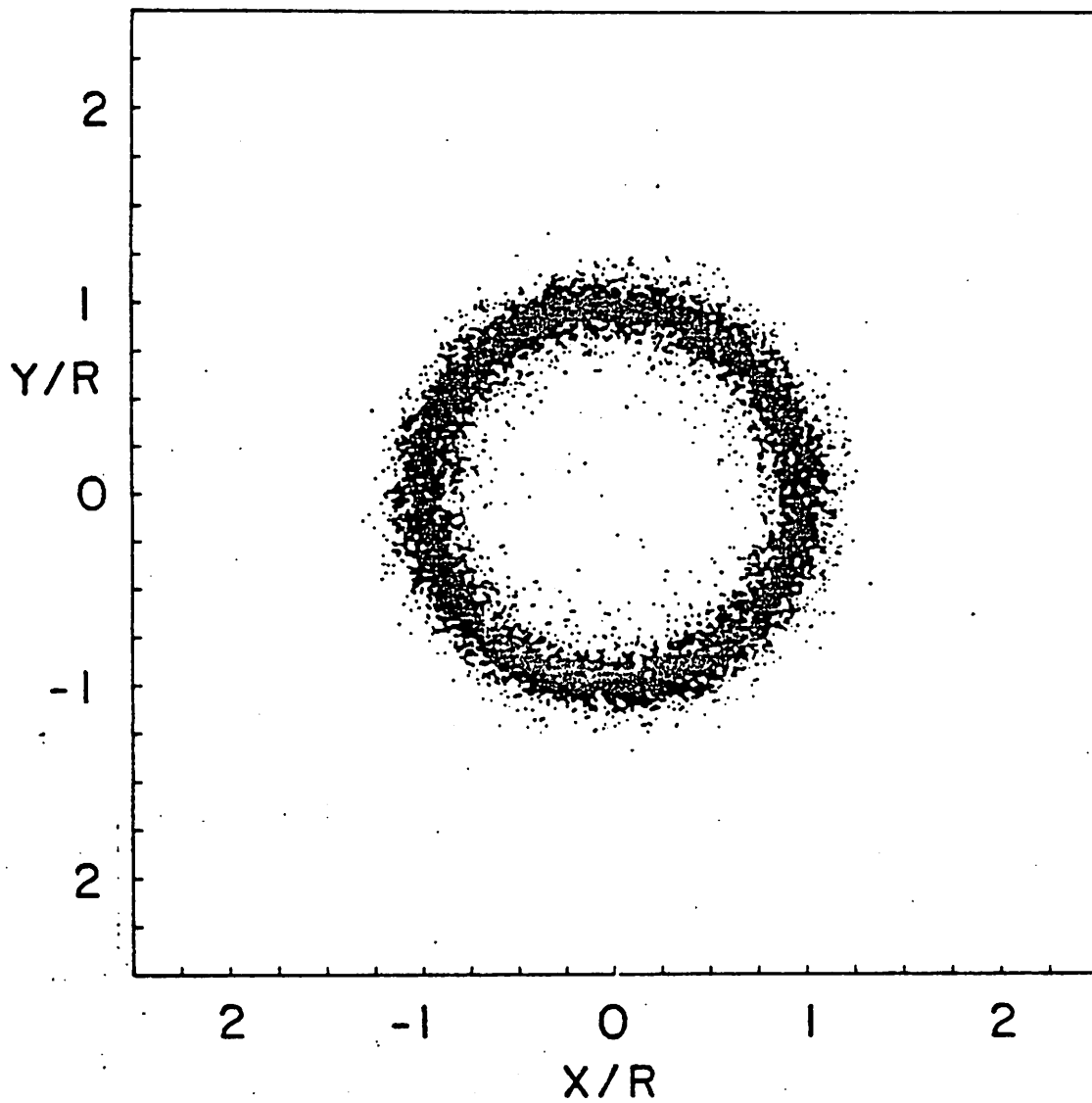


FIG. 5. Initial particle positions for an ion layer unstable to $m=2$ and $m=3$ modes.
 $R/a=5$ and $\zeta=1.1$.

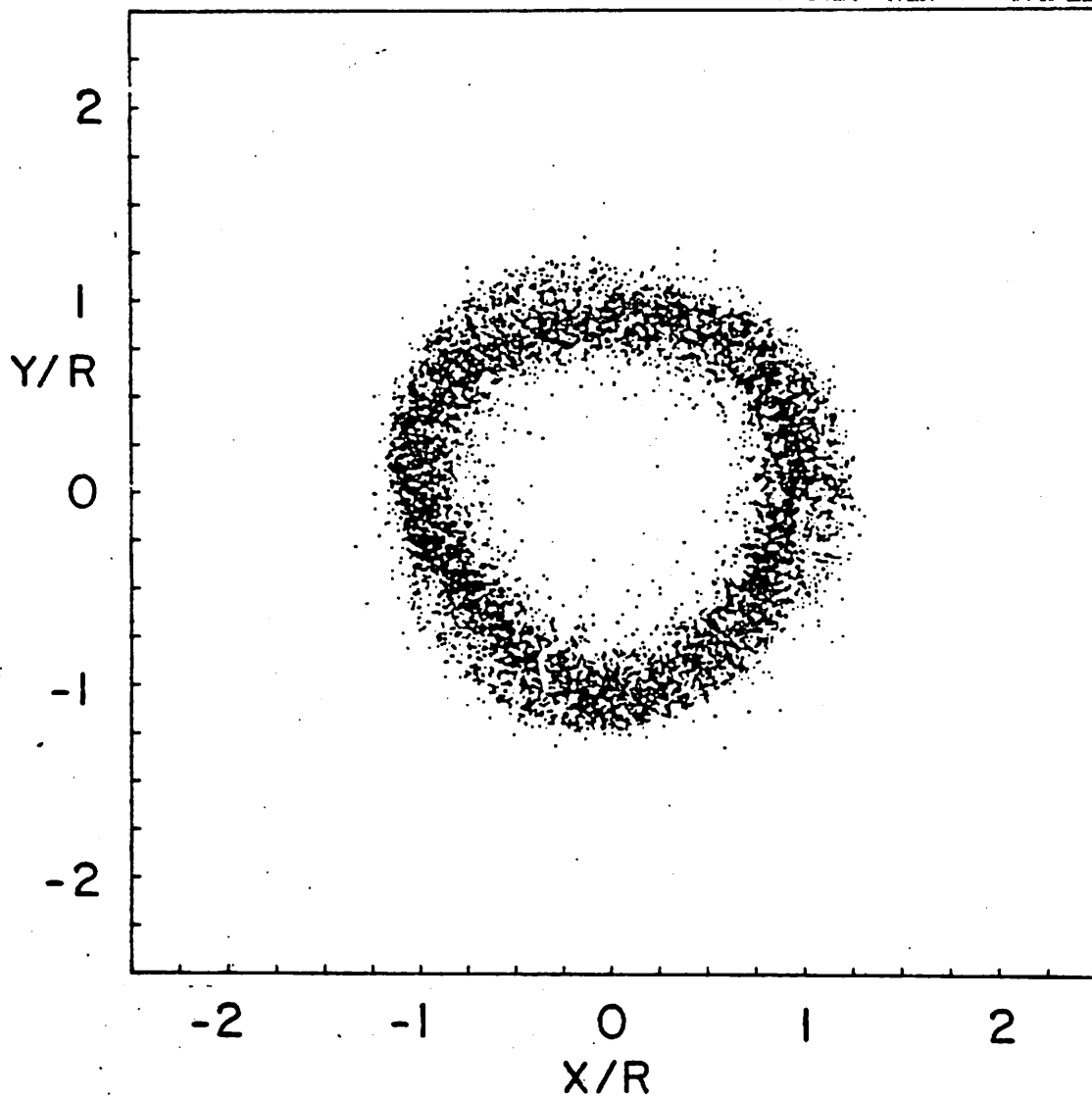


FIG. 6. Particle positions at $t=50\omega_{ci}^{-1}$, after an $m=3$ instability has grown to large amplitude.

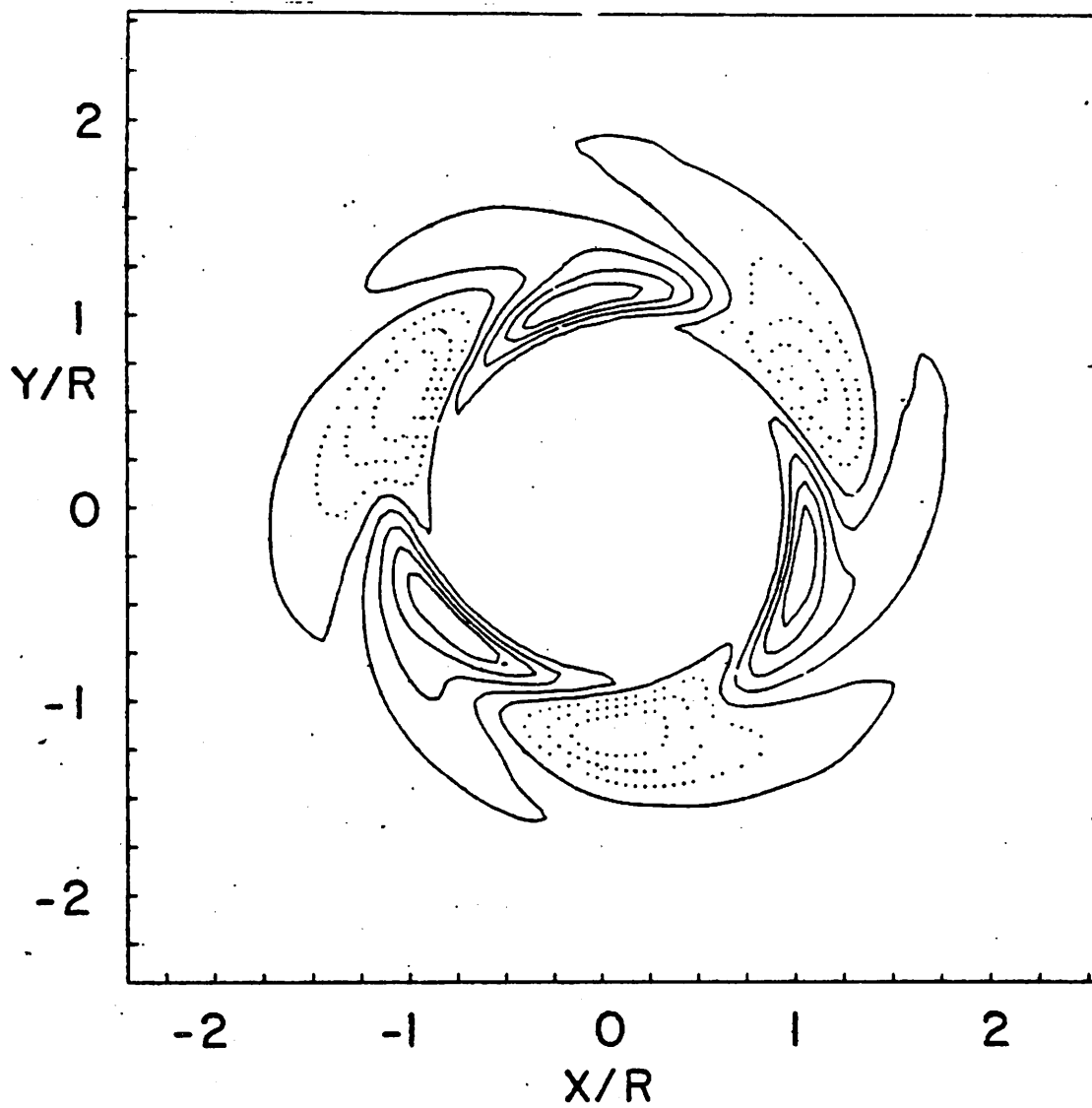


FIG. 7. Contours of E_θ at $t=50\omega_{ci}^{-1}$, showing the $m=3$ structure. Dotted lines represent $E_\theta < 0$ and solid lines represent $E_\theta \geq 0$.

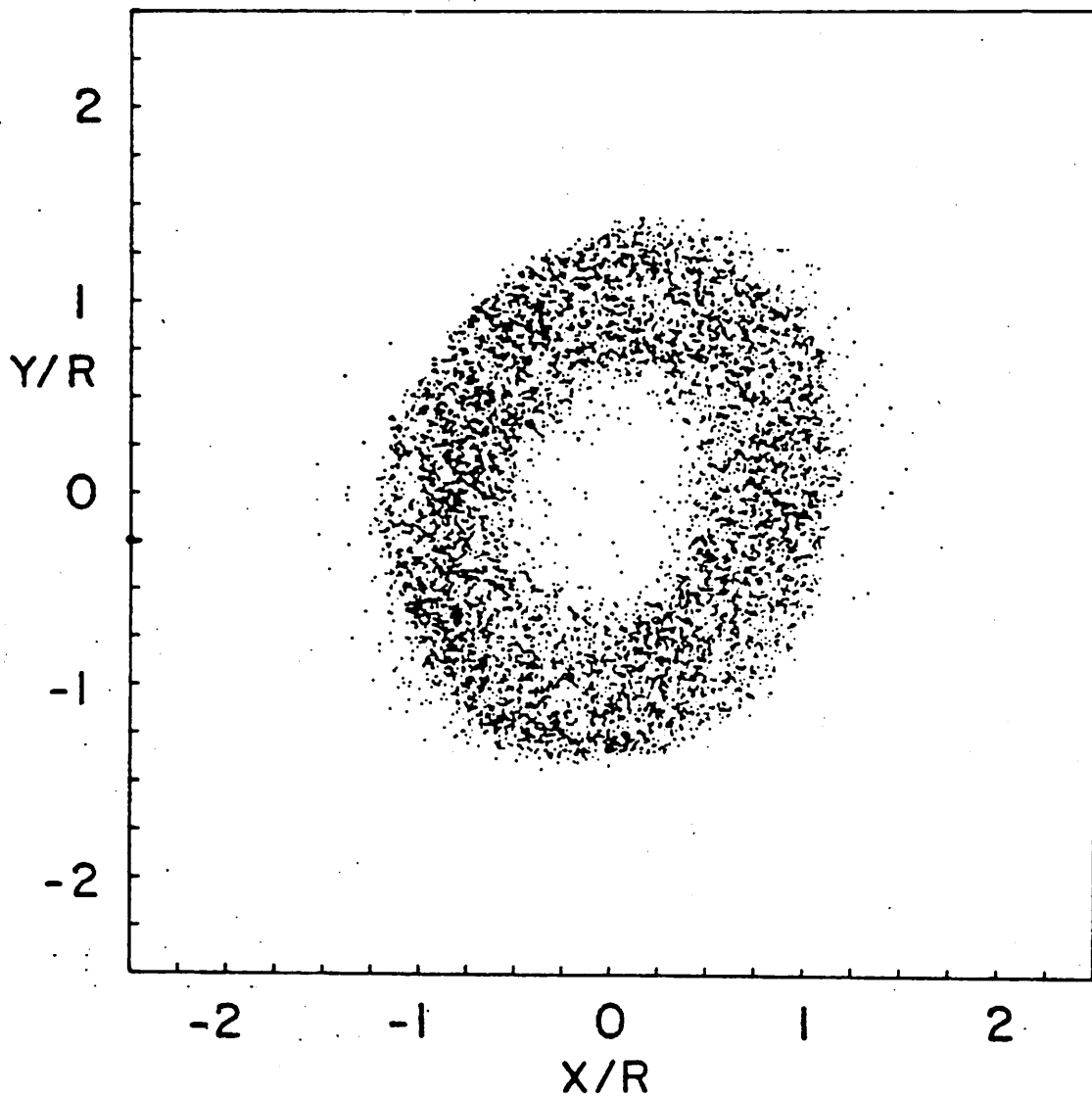


FIG. 8. Particle positions at $t=100\omega_{ci}^{-1}$. An $m=2$ instability now dominates.

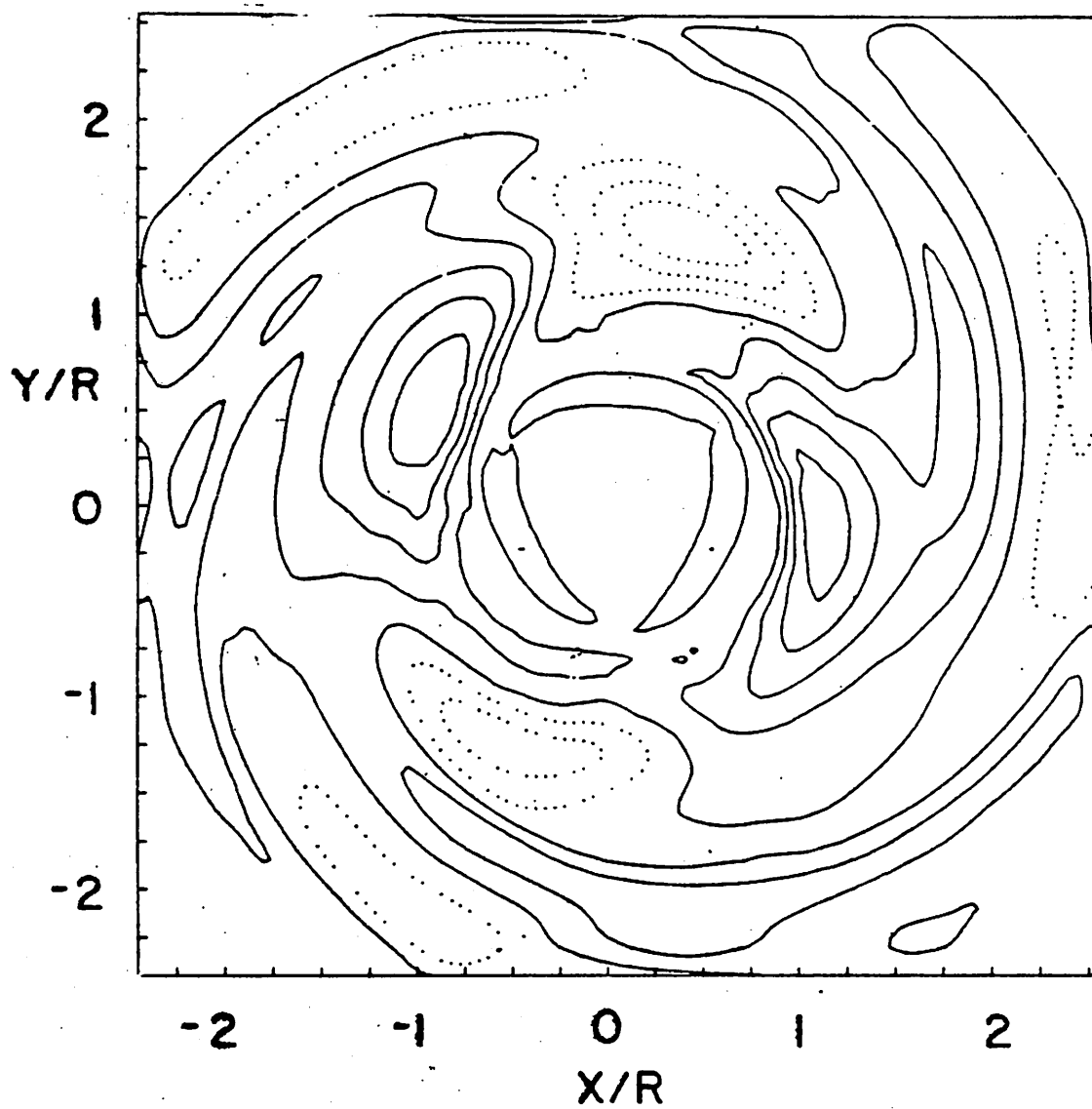


FIG. 9. Contours of E_θ at $t=100\omega_{ci}^{-1}$, showing $m=2$ structure. Dotted lines represent $E_\theta < 0$ and solid lines represent $E_\theta \geq 0$.

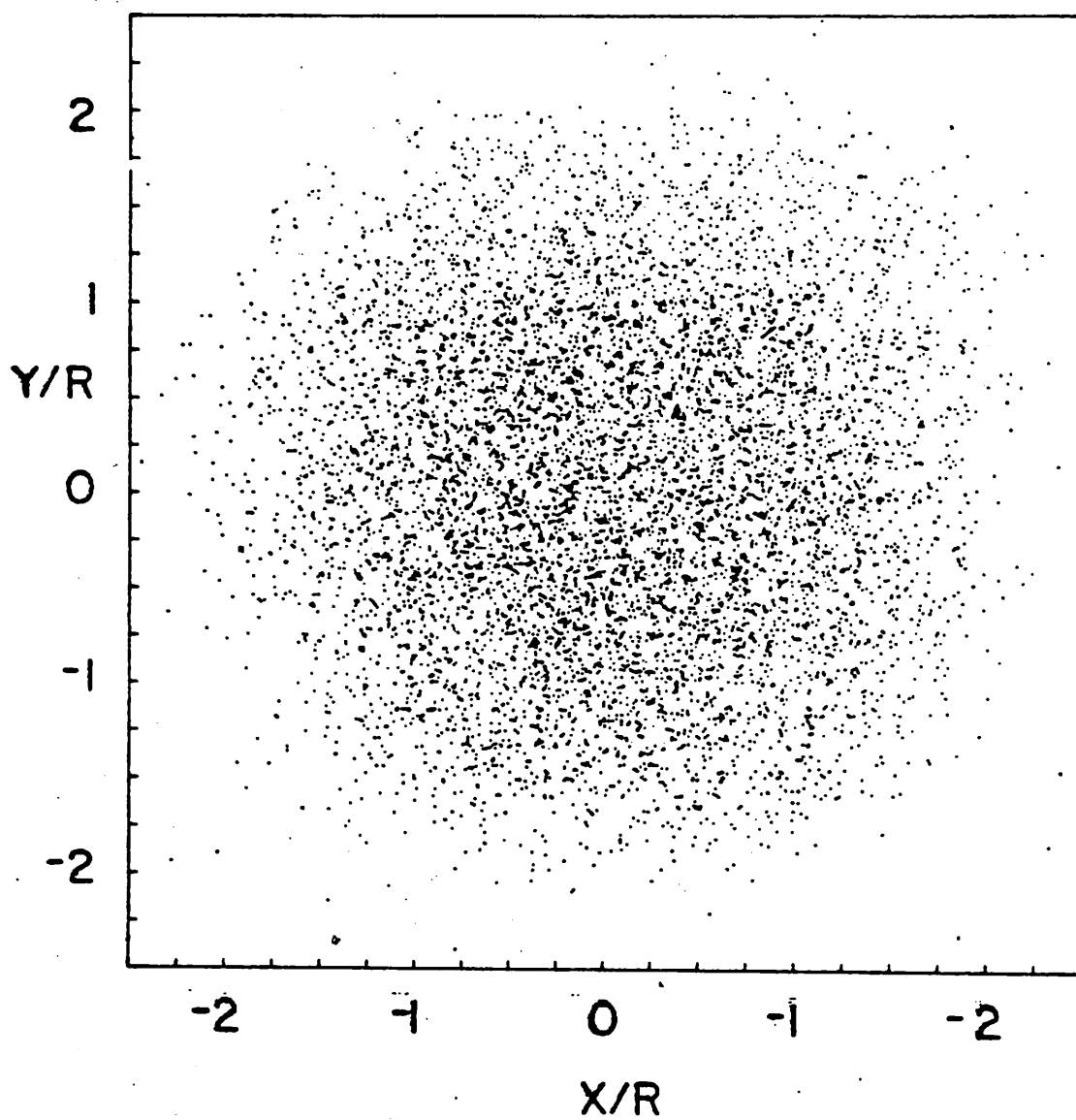


FIG. 10. Particle positions at $t=300\omega_{ci}^{-1}$, after all instabilities appear to have saturated.

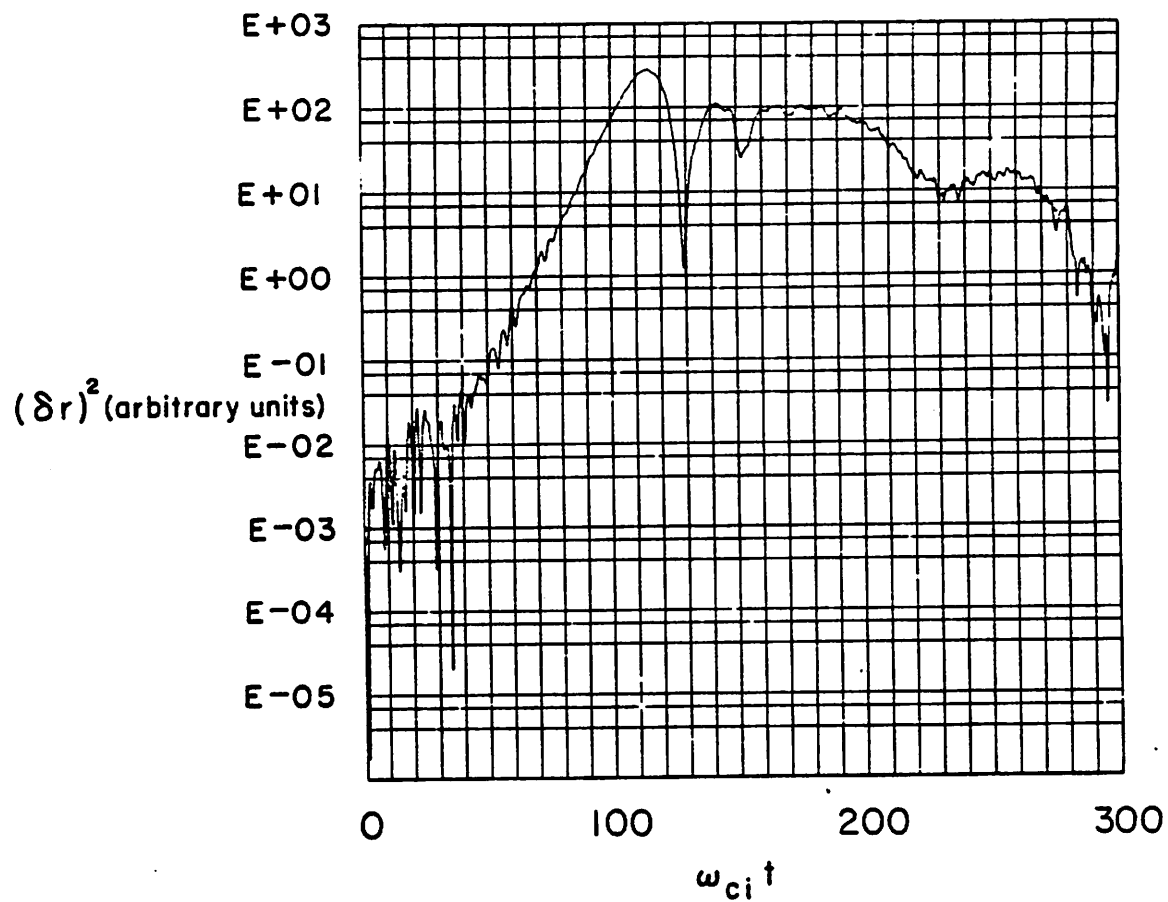


FIG. 11. $(\delta r)^2$ for mode 2 as a function of time.

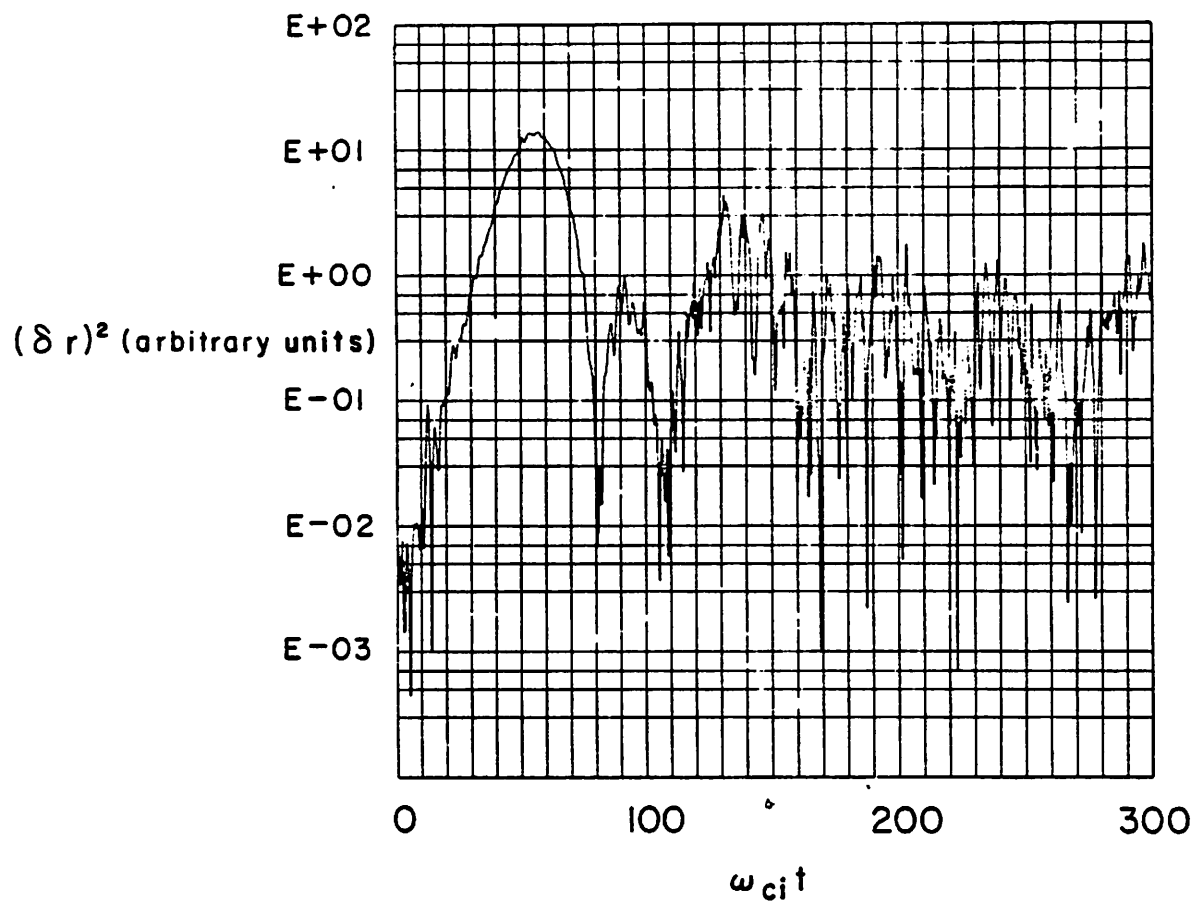


FIG. 12. $(\delta r)^2$ for mode 3 as a function of time.

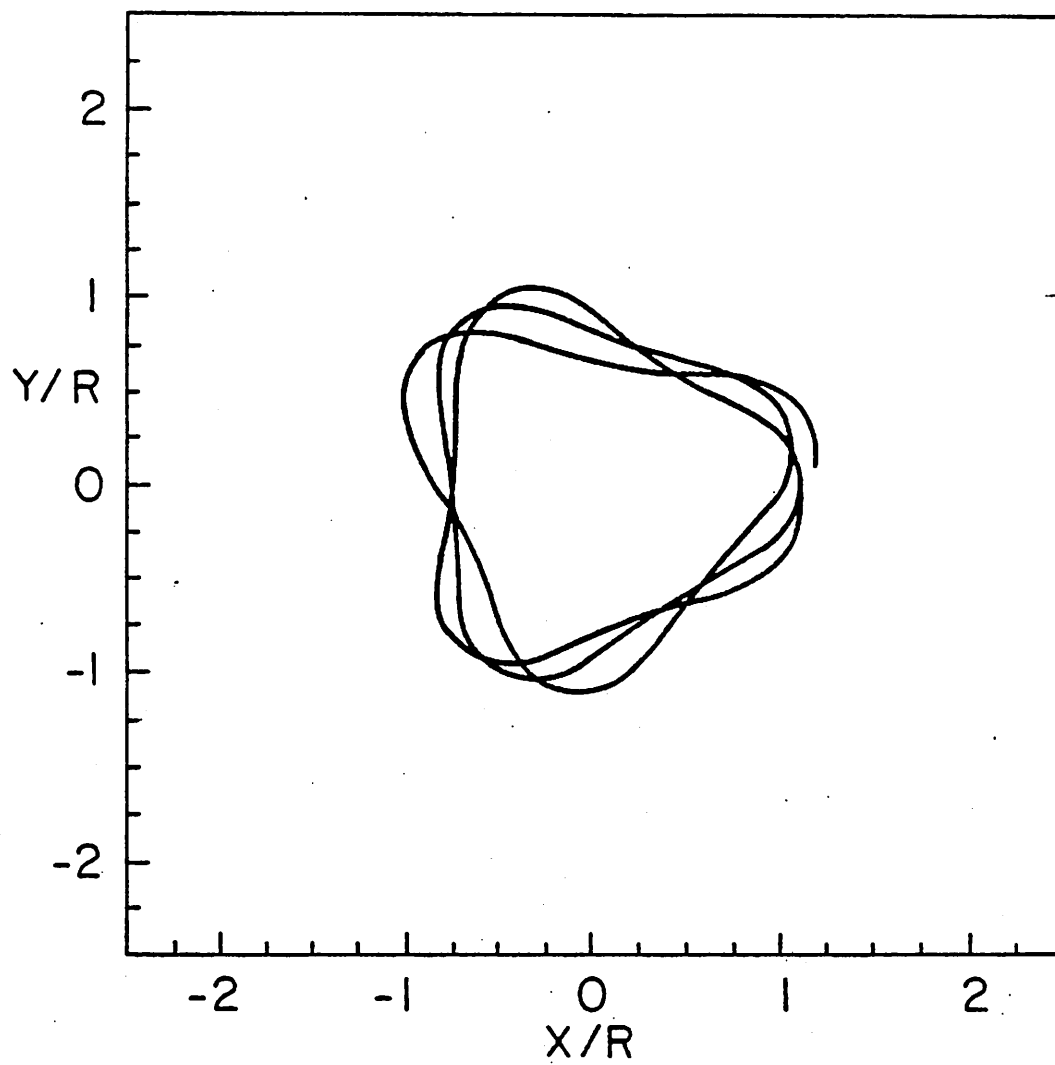


FIG. 13. A typical particle trajectory from $t=0$ to $t=60\omega_{ci}^{-1}$.

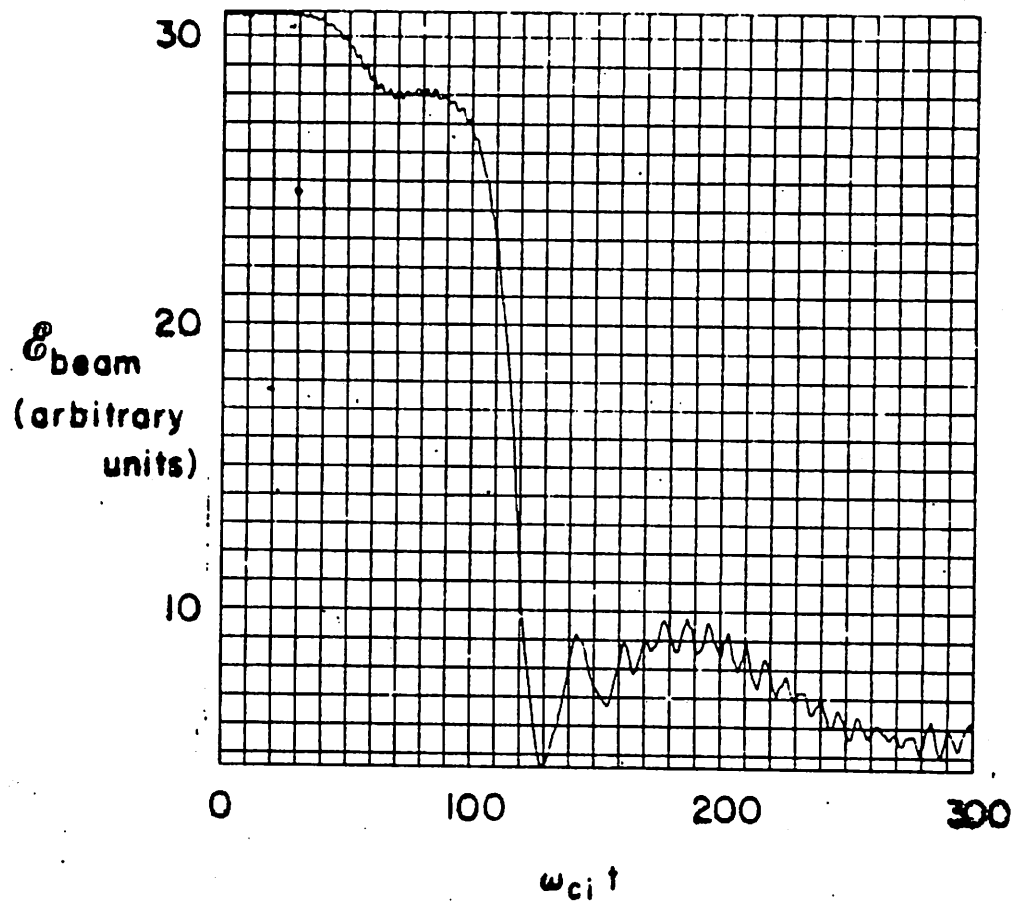


FIG. 14. Directed beam energy, $\sum_i M_{b,i} \bar{v}_\theta^2$, where the summation is over all beam particles, as a function of time, showing the loss of directed energy during instability growth.

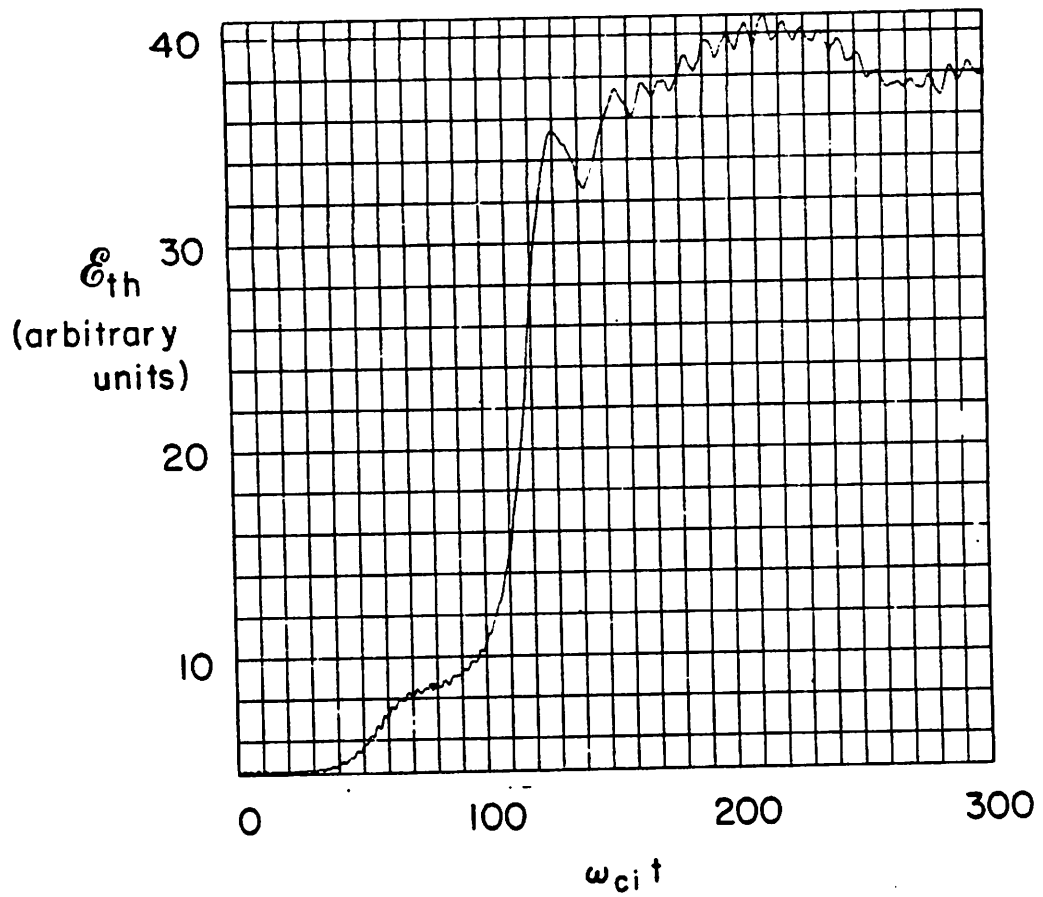


FIG. 15. Beam thermal energy, $\sum_i \frac{1}{2} M_{b,i} [(v_{\theta,i} - \bar{v}_{\theta})^2 + v_{r,i}^2]$, where the summation is over all particles, as a function of time, showing the beam heating during instability growth.

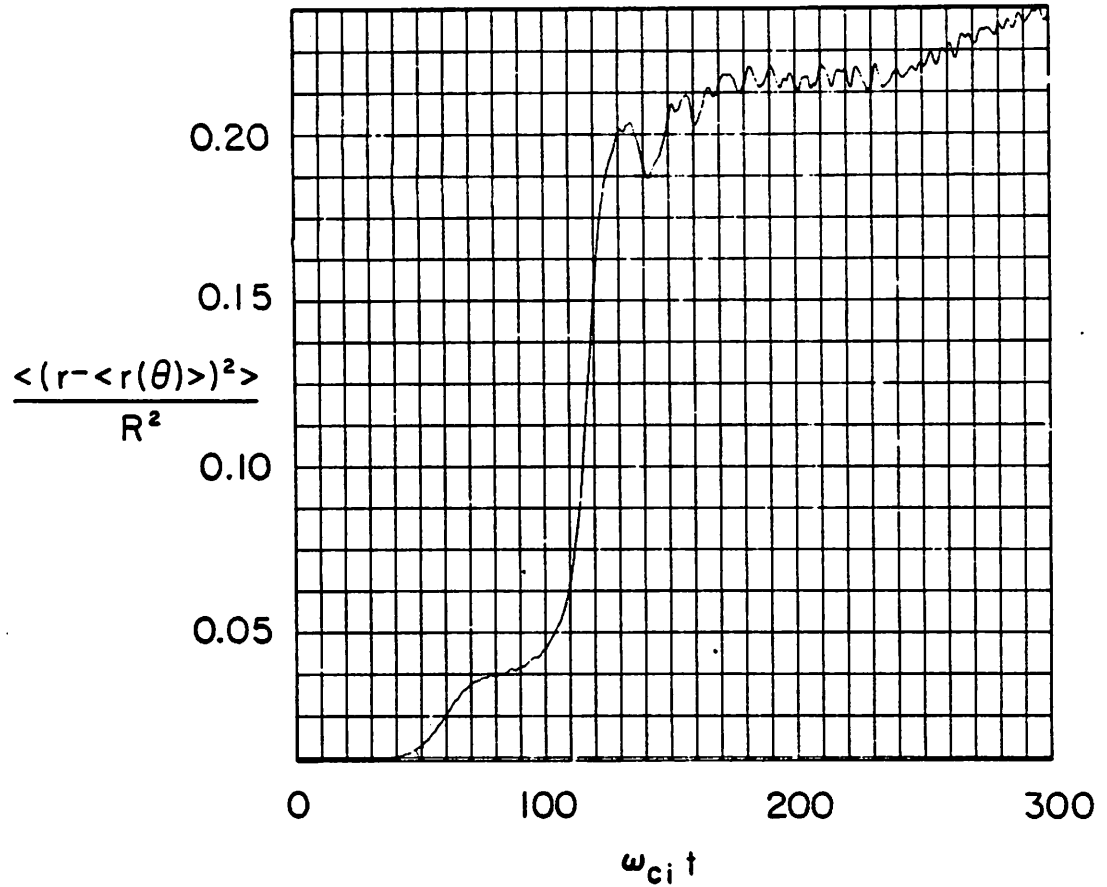


FIG. 16. $\langle (r - \langle r(\theta) \rangle)^2 \rangle$ as a function of time, showing the layer expansion. The expansion from $t=0$ to $t=60\omega_{ci}^{-1}$ is due to the $m=3$ instability. At later times, from $t=60\omega_{ci}^{-1}$ to $t=140\omega_{ci}^{-1}$, the expansion is due to the $m=2$ instability.

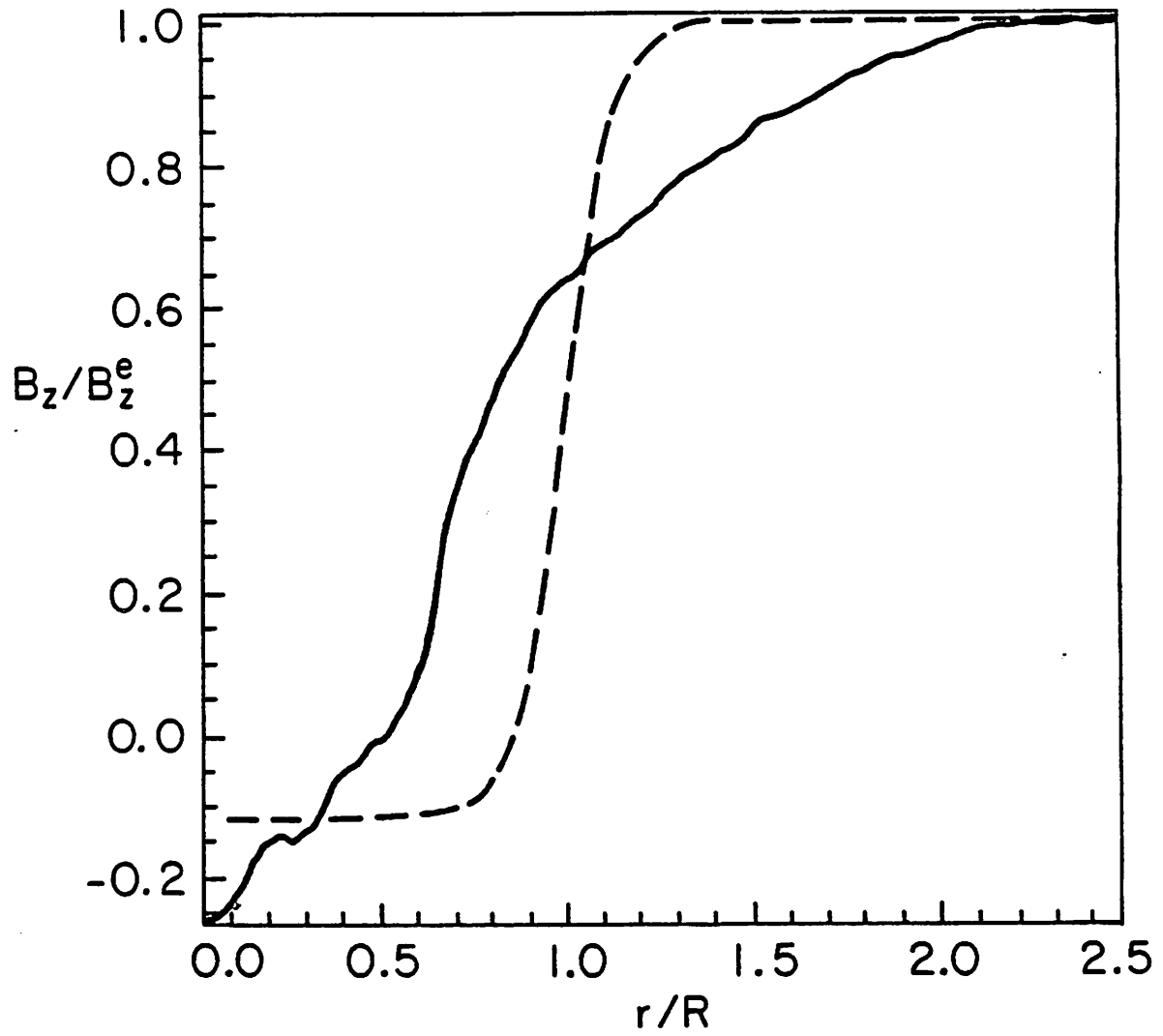


FIG. 17. Magnetic field profiles, $B_z(r)$ averaged over θ , at $t=0$ (dotted line) and at $t=300\omega_{ci}^{-1}$, after instabilities have saturated (solid line).

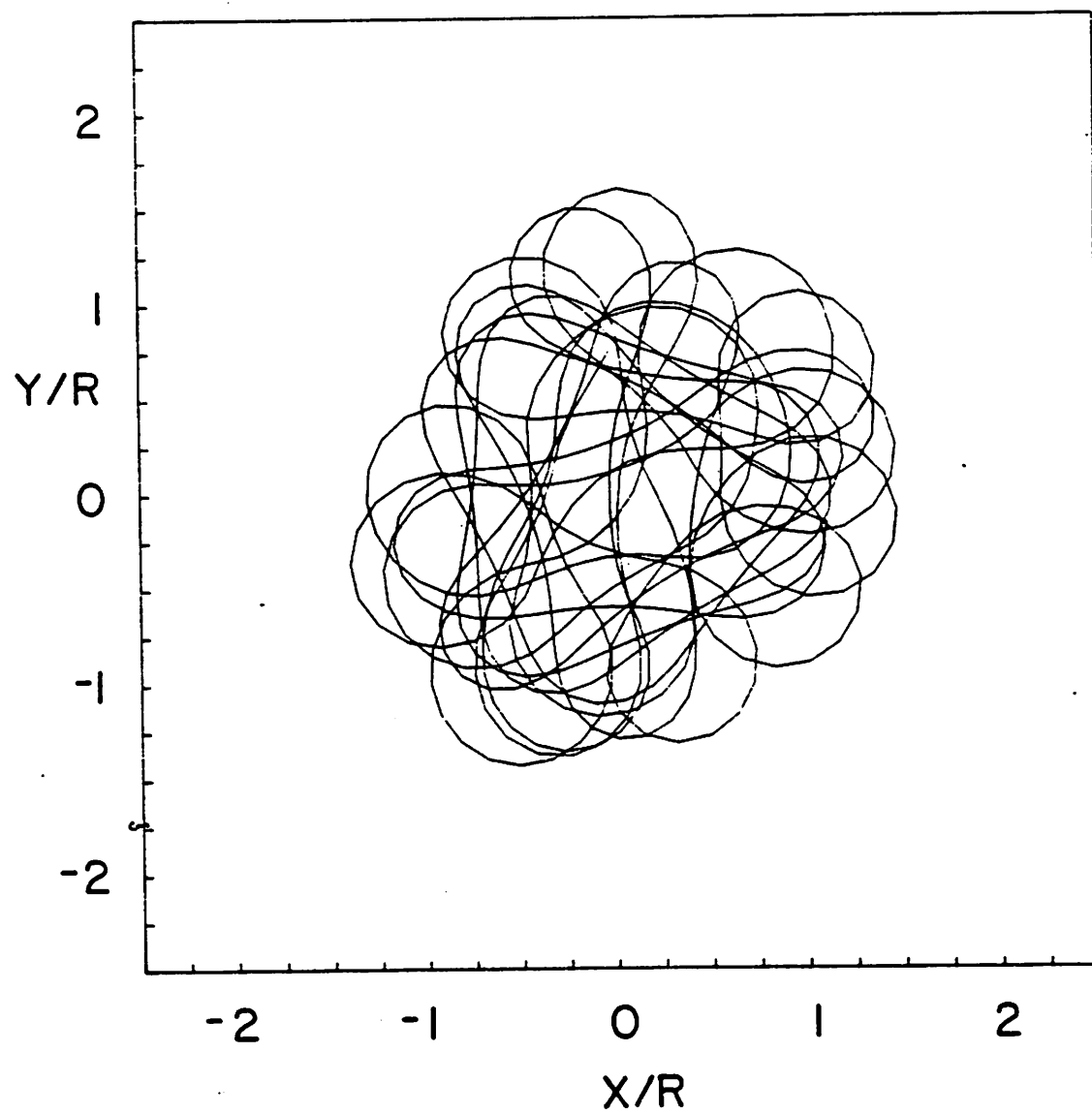


FIG. 18. Particle trajectory, for the particle shown in Fig. 13, from $t=0$ to $t=300\omega_{ci}^{-1}$.

A.1 Numerical Calculation of Linear Growth Rates for Ion

Layer Kink Instabilities

This appendix describes the procedure used to calculate numerically the complex frequencies from the equations of Lovelace¹. Assuming perturbations of the form $\bar{\epsilon}_r(\theta, t) = \hat{r}\epsilon_r \exp(im\theta - i\omega t)$ Eq. 1a can be written as

$$(m^2\Omega^2 - 2m\Omega\omega + \omega^2)\epsilon_r = -\Omega^2(1 + \eta_s)\epsilon_r + \delta F_r. \quad (\text{A.1})$$

The radial perturbation is rigid, i.e. $\epsilon_r = \epsilon_r(\theta, t)$. With this assumption, Eq. 1a then becomes

$$f(\omega) = -m^2\Omega^2 + 2m\Omega\omega - \omega^2 - \Omega^2(1 + \eta_s) + \frac{1}{\epsilon_r}\delta F_r = 0 \quad (\text{A.2})$$

The object is to find the complex roots, ω , of Eq. A.2. This process would be straightforward, except for the fact that δF_r is a complicated function of ω , involving integration over the radial thickness of the layer and the solution of a second order differential equation.

If a guess is made for the complex frequency, the following method will determine the corresponding value of $(1/\epsilon_r)\delta F_r$. With the known rigid rotor profiles for the current density and magnetic field, one can obtain $\Lambda_a(r)$, $\Lambda_b(r)$, and $\phi'(r)$ from

$$\Lambda_a = \left(\frac{v_A}{c}\right)^2 \frac{1 + (v_A/c)^2}{(1 + (v_A/c)^2)^2 - (\omega/\omega_{ci})^2} \quad (\text{A.3a})$$

$$\Lambda_b = \left(\frac{v_A}{c}\right)^2 \frac{i\omega}{(1 + (v_A/c)^2)^2 - (\omega/\omega_{ci})^2} \quad (\text{A.3b})$$

$$\phi' \equiv \frac{\phi}{\epsilon_r} = \left(\frac{\omega r}{m\bar{v}_\theta} \right) 4\pi J_b / c \quad (\text{A.3c})$$

It is then possible to solve for $\Delta B'_z$ from the second order differential equation

$$\begin{aligned} \frac{1}{r} \frac{\partial}{\partial r} \left(r \Lambda_a \frac{\partial}{\partial r} \Delta B'_z \right) + \left(\frac{\omega^2}{c^2} - \frac{m^2 \Lambda_a}{r^2} \right) \Delta B'_z - \frac{in}{r} \left(\frac{\partial}{\partial r} \Lambda_b \right) \Delta B'_z \\ = \left(\frac{m^2 \Lambda_a}{r^2} - \frac{\omega m \bar{v}_\theta}{c^2 r} \right) \phi' - \frac{1}{r} \frac{\partial}{\partial r} (\Lambda_a \phi') + \frac{\partial}{\partial r} \left(\frac{im \Lambda_b \phi'}{r} \right). \end{aligned} \quad (\text{A.4})$$

At the conducting wall at $r=r_w$ we have the boundary condition

$$\left(\frac{1}{\Delta B'_z} \frac{\partial}{\partial r} \Delta B'_z \right)_{r=r_w} = \frac{im \Lambda_b(r_w)}{r_w \Lambda_a(r_w)} \quad (\text{A.5})$$

and at $r=0$, $\Delta B'_z(0)=0$. This is a second order two-point boundary value problem and is solved by finite difference methods. Once $\Delta B'_z$ is determined it is possible to obtain δB_z , δE_r , and δE_θ from

$$\frac{\delta B_z}{\epsilon_r} = \Delta B'_z + \frac{4\pi}{c} J_b \quad (\text{A.6a})$$

$$\frac{i\omega}{c} \frac{\delta E_r}{\epsilon_r} = -\Lambda_a \frac{im}{r} (\Delta B'_z + \phi') - \Lambda_b \left(\frac{\partial}{\partial r} \Delta B'_z + \frac{\phi'}{r} \right) \quad (\text{A.6b})$$

$$\frac{i\omega}{c} \frac{\delta E_\theta}{\epsilon_r} = -\Lambda_b \frac{im}{r} (\Delta B'_z + \phi') + \Lambda_a \left(\frac{\partial}{\partial r} \Delta B'_z + \frac{\phi'}{r} \right) \quad (\text{A.6c})$$

The quantities η_s , $\langle \delta B_z \rangle$, $\langle \delta E_r \rangle$, and $\langle \delta E_\theta \rangle$, which are used in δF_r , are evaluated by numerical integration over the layer using expression for the average,

$$\langle (\dots) \rangle \equiv \int r dr J_b(r) (\dots) / \int r dr J_b(r).$$

Then, using

$$\frac{1}{\epsilon_r} \delta F_r = \frac{q\bar{v}_\theta}{M_b c} \frac{1}{\epsilon_r} \langle \delta B_z \rangle + \frac{q}{M_b} \frac{1}{\epsilon_r} \langle \delta E_r \rangle - \frac{iq}{M_b m} \frac{1}{\epsilon_r} \langle \delta E_\theta \rangle, \quad (\text{A.7})$$

all of the terms in Eq. A.2 are now known for the given frequency guess.

The above procedure is repeated for each guess of ω as a function call in a Muller's method² subroutine. Muller's method will provide guesses for the complex

roots of $f(\omega)$ in Eq. A.2 until the given convergence criteria are met. The Muller's method subroutine used in this code is based on a subroutine written by Au-Yeung and Friedman³.

References

1. R.V. Lovelace, "Precession and Kink Motion of Long Astron Layers", *Phys. Fluids* **22**, pp. 708-717 (1979).
2. S.D. Conte and C. de Boor, *Elementary Numerical Analysis: An Algorithmic Approach*, Ed. 2, pp. 74-83, McGraw-Hill (New York, 1972).
3. H.S. Au-Yeung and A. Friedman, "Solver: An Analytic Function Root Solving and Plotting Package", Univ. of Calif., Berkeley, Electronics Research Laboratory Report UCB/ERL-M79/55 (1979).

A.2 Further Results of Ion Layer Kink Instability Simulations

This appendix presents results from two runs which demonstrate the effects of increasing field-reversal and decreasing layer thickness on ion layer kink instabilities.

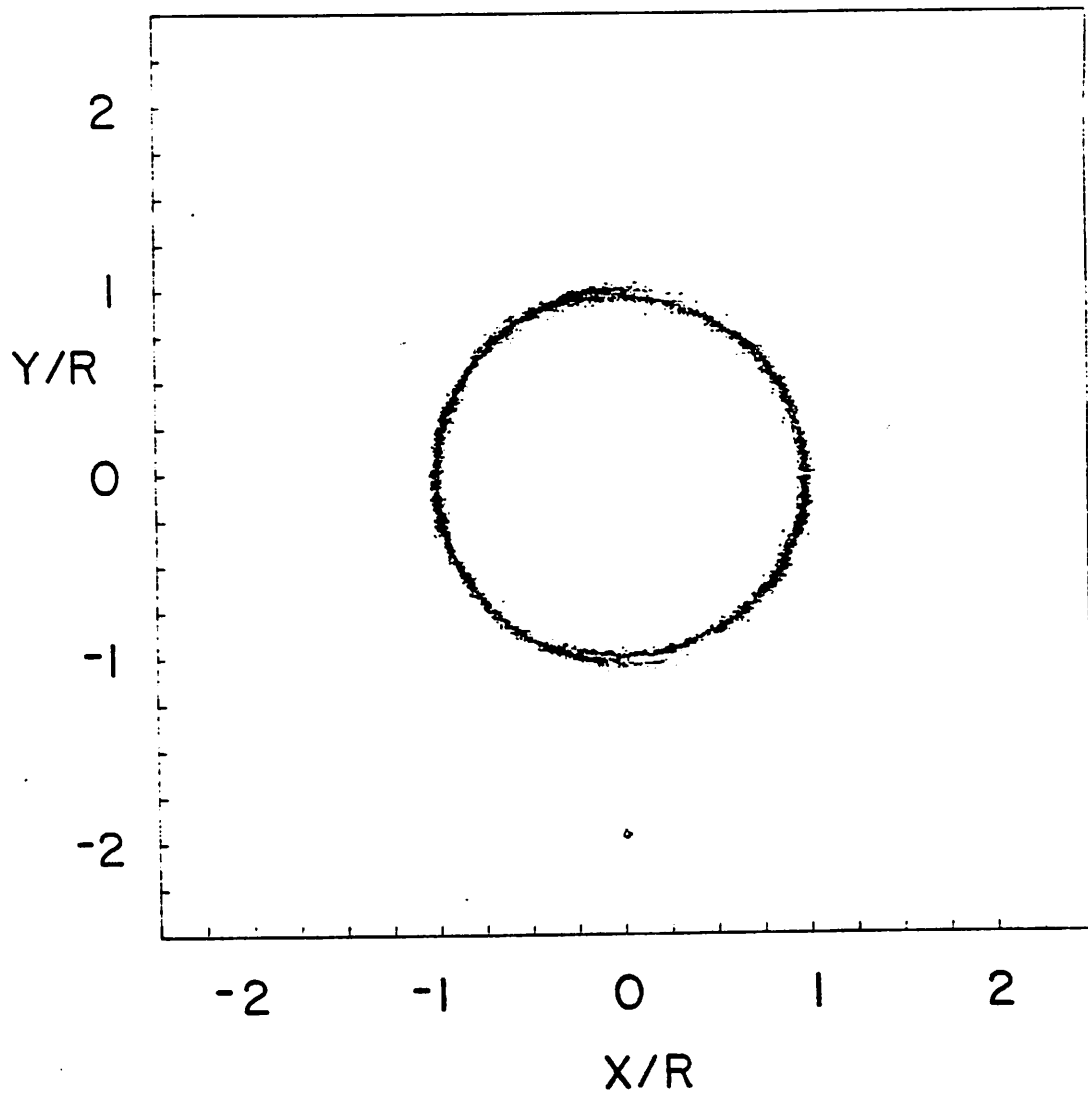
1. Decreased Layer Thickness

In this simulation we use the same background density and field-reversal as used in the run described in detail in the main section, i.e., $v_A/a\omega_{ci}=0.1$ and $\zeta=1.1$. However, we reduce the initial layer thickness so that $R/a=10$ rather than 6. This has the effect of increasing the self-magnetic field index from $\eta_s=5.9$ to $\eta_s=13.0$. This value of η_s is slightly larger than the threshold for the $m=5$ mode. Therefore, we expect modes 2, 3, 4, and 5 to be unstable. Our simulation results confirm this. The growth of the $m=5$ mode is relatively small and is not evident in the snapshot diagnostics. Figure 1 shows the initial particle positions for this thin layer. In Fig. 2, at $t=30\omega_{ci}^{-1}$, an $m=4$ instability is apparent, as expected, since its growth rate is the largest of the unstable modes. This mode ceases to grow at $t=36\omega_{ci}^{-1}$. The $m=3$ mode, having a smaller growth rate than the $m=4$ mode, continues to grow and its amplitude eventually exceeds the amplitude of the $m=4$ mode. This can be seen in Fig. 3 at $t=70\omega_{ci}^{-1}$. At a considerably later time, $t=130\omega_{ci}^{-1}$, the $m=2$ mode dominates, as is clear from Fig. 4. The time evolution of $(\delta r)^2$ is plotted in Figs. 5-8 for these modes. Figure 9 shows the change in $\langle (r - \langle r(\theta) \rangle)^2 \rangle$ with time. The increase in layer thickness due to each of the modes, $m=2, 3$, and 4, can be seen in this figure. Although this run is

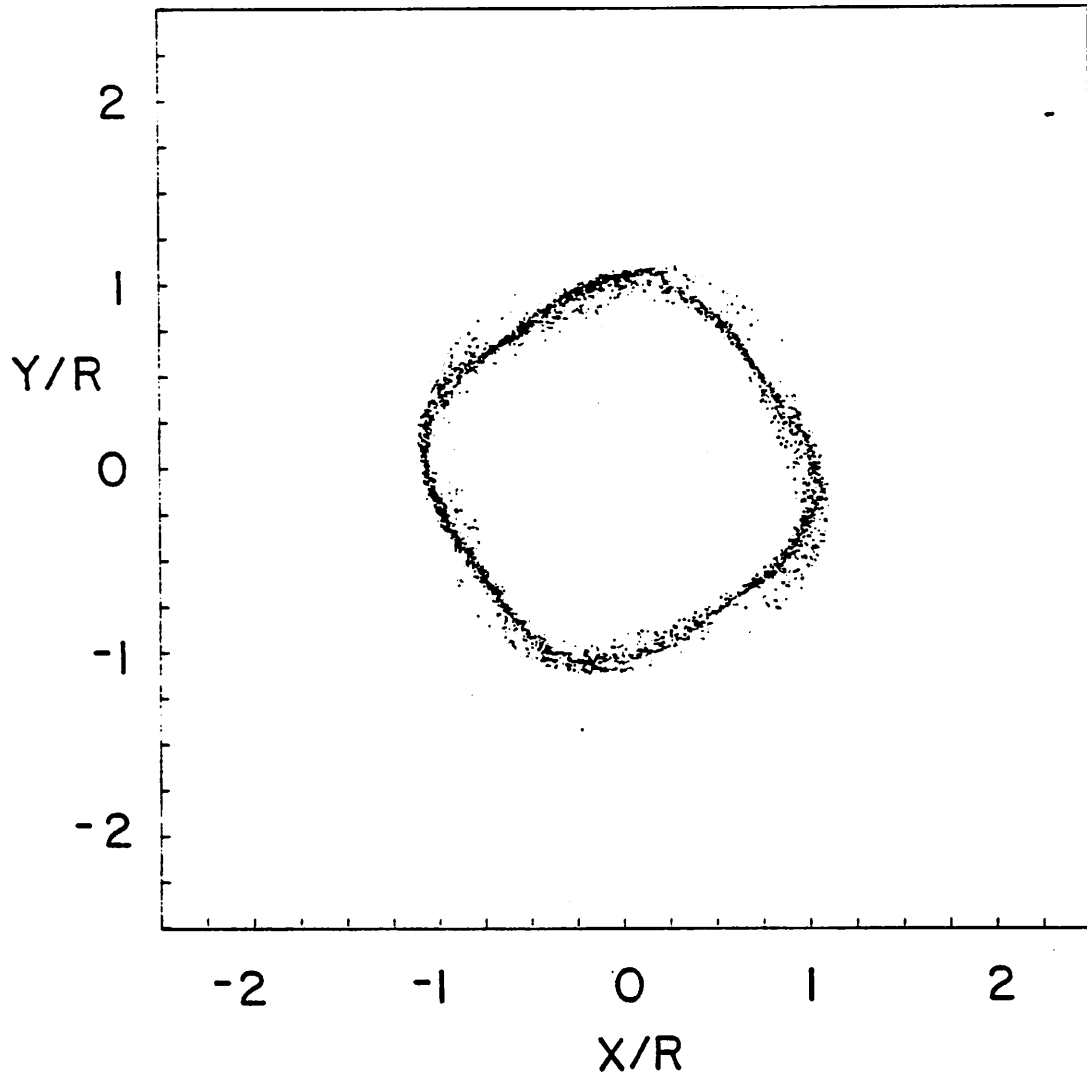
not as long as the one described in the main section, note that at $t=220\omega_{ci}^{-1}$, after all modes have saturated, the magnitude of $\langle (r - \langle r(\theta) \rangle)^2 \rangle$ at a comparable time is approximately the same, indicating that the only effect of making a layer thinner is that it must proceed through the saturation of more instabilities before it reaches the eventual thick layer state.

2. Increased Field-Reversal

This run has the same background plasma density as the run discussed in the main section. The layer thickness is slightly larger, $R/a=5$ rather than 6. The primary difference is that the degree of field-reversal has been increased from $\zeta=1.1$ to $\zeta=1.38$. This has the effect of increasing the self-magnetic field index from $\eta_s=5.9$ to $\eta_s=12.3$. This value is sufficiently large so that the $m=4$ mode will be unstable in addition to the $m=2$ and $m=3$ modes. Figure 10 shows the initial particle positions for this layer. Figure 11 shows the layer at $t=50\omega_{ci}^{-1}$, after an $m=4$ instability has grown to large amplitude. In Fig. 12, at $t=70\omega_{ci}^{-1}$, the $m=4$ mode has saturated and the $m=3$ mode now dominates. Finally, in Fig. 13, at $t=220\omega_{ci}^{-1}$, after the exponential growth of all modes has stopped, some $m=2$ structure still remains due to the growth of the last unstable mode, the $m=2$ mode. This run ended at this point; however, from the results of other similar runs, such as the one described in the main section, we would expect this structure to eventually disappear. Figure 14 shows the change in the magnetic field profile. Note that field-reversal is maintained.



FIGA1 Initial particle positions for thin layer, $(R/a)=10$, $\zeta=1.1$.



FIGA2 Particle positions at $t=30\omega_{ci}^{-1}$, after an $m=4$ instability has become apparent.

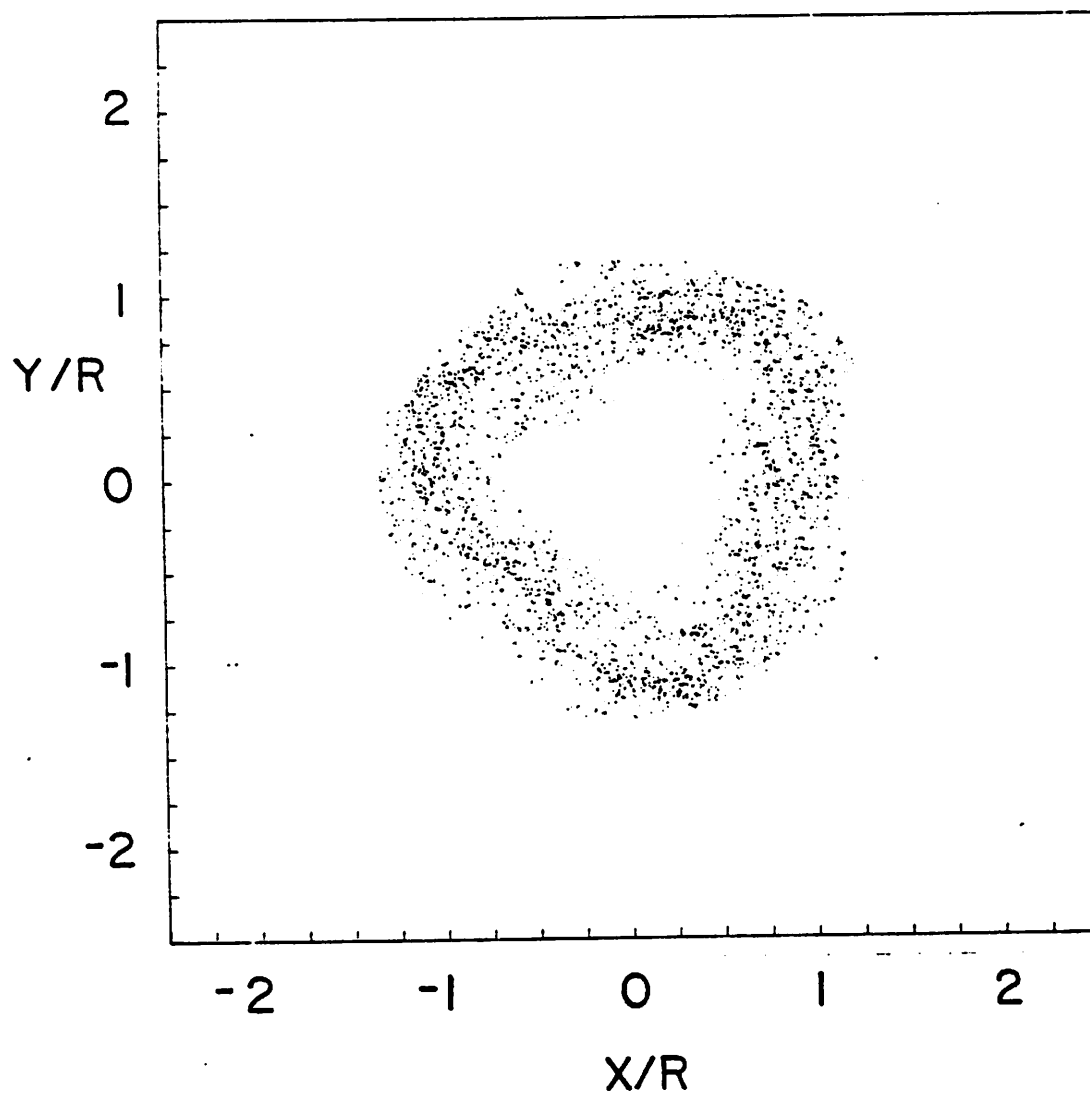


FIG.A3 Particle positions at $t=70\omega_{ci}^{-1}$. The layer has thickened and now an $m=3$ instability dominates.

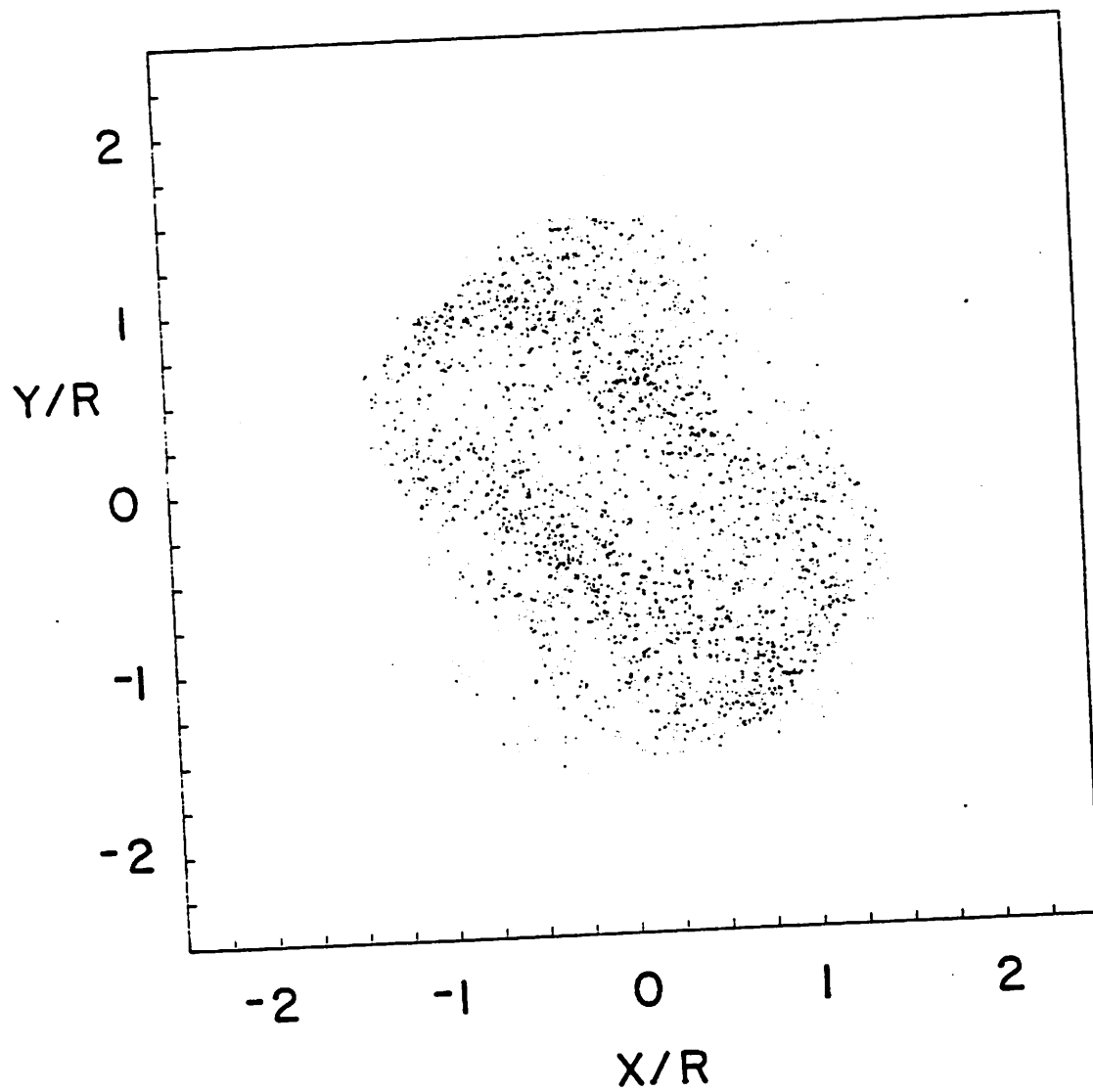


FIG. A4 Particle positions at $t=130\omega_{ci}^{-1}$. The $m=2$ mode now dominates.

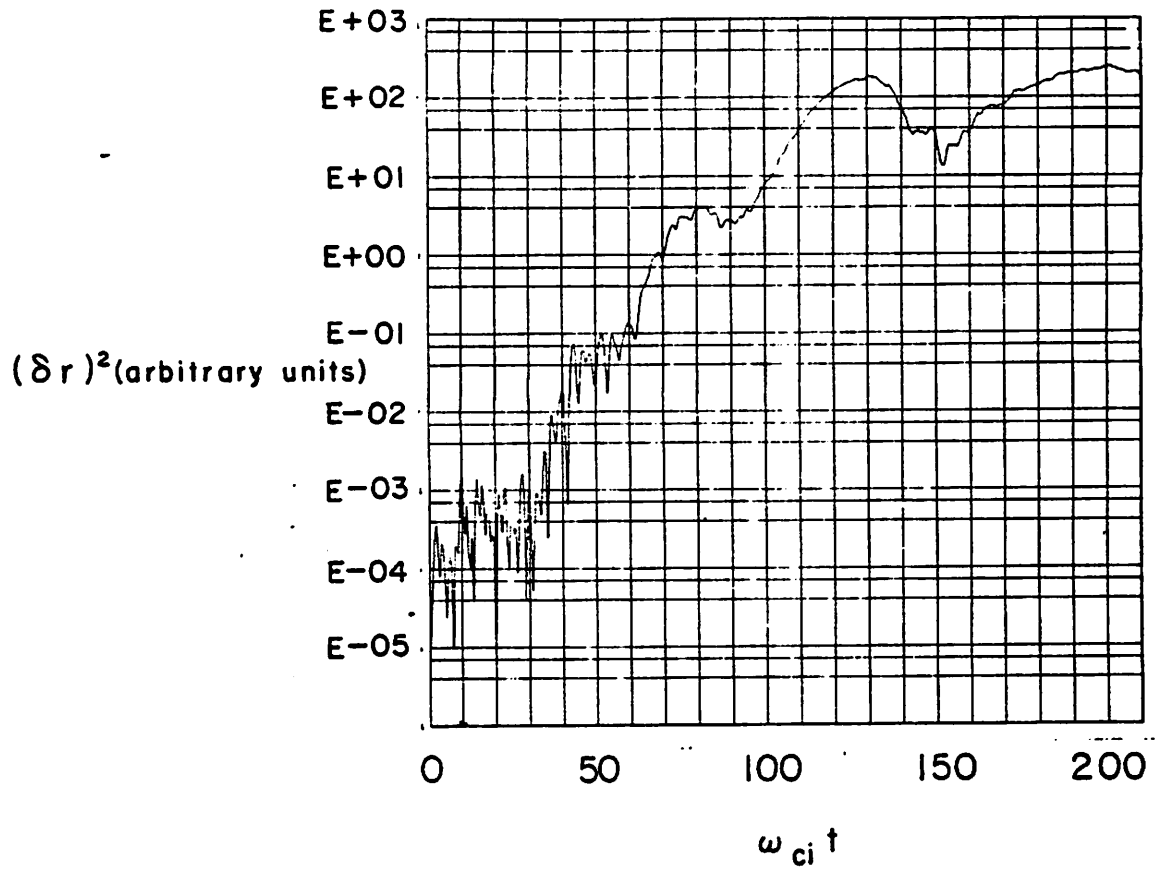


FIG. 5 $(\delta r)^2$ as a function of time for the $m=2$ mode.

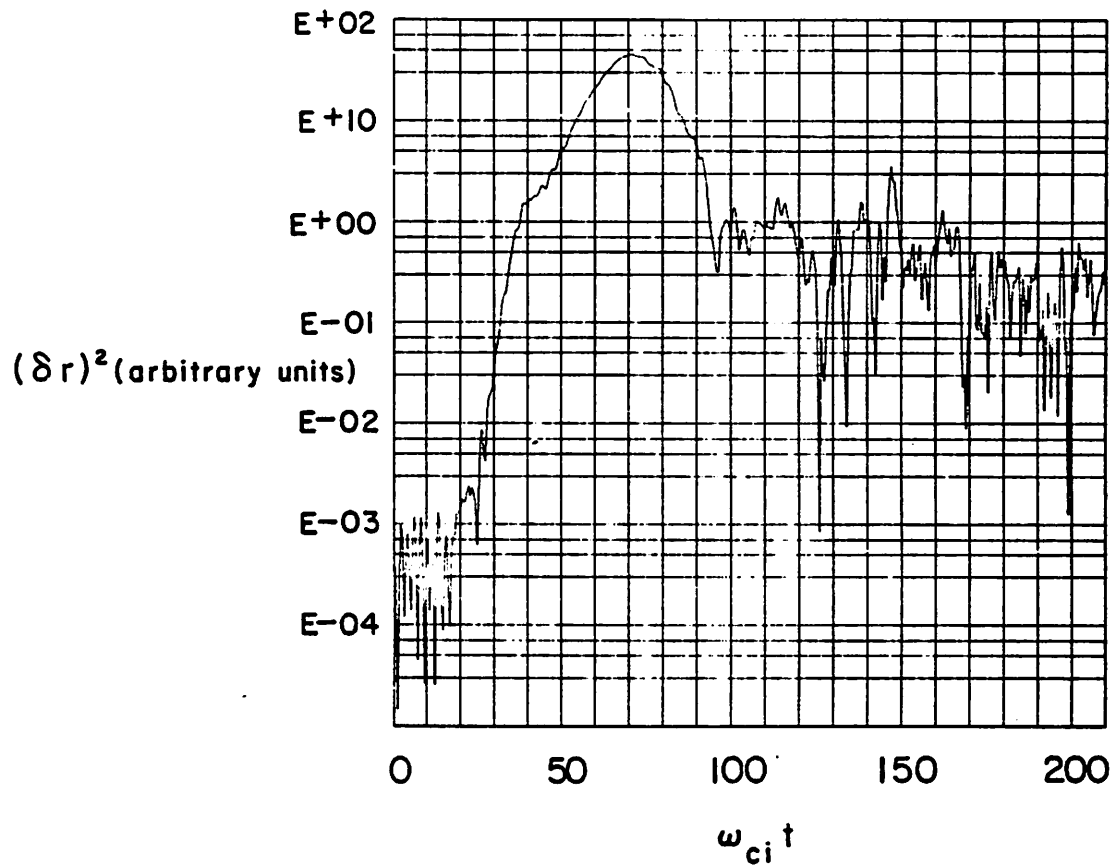


FIG. A6 $(\delta r)^2$ as a function of time for the $m=3$ mode.

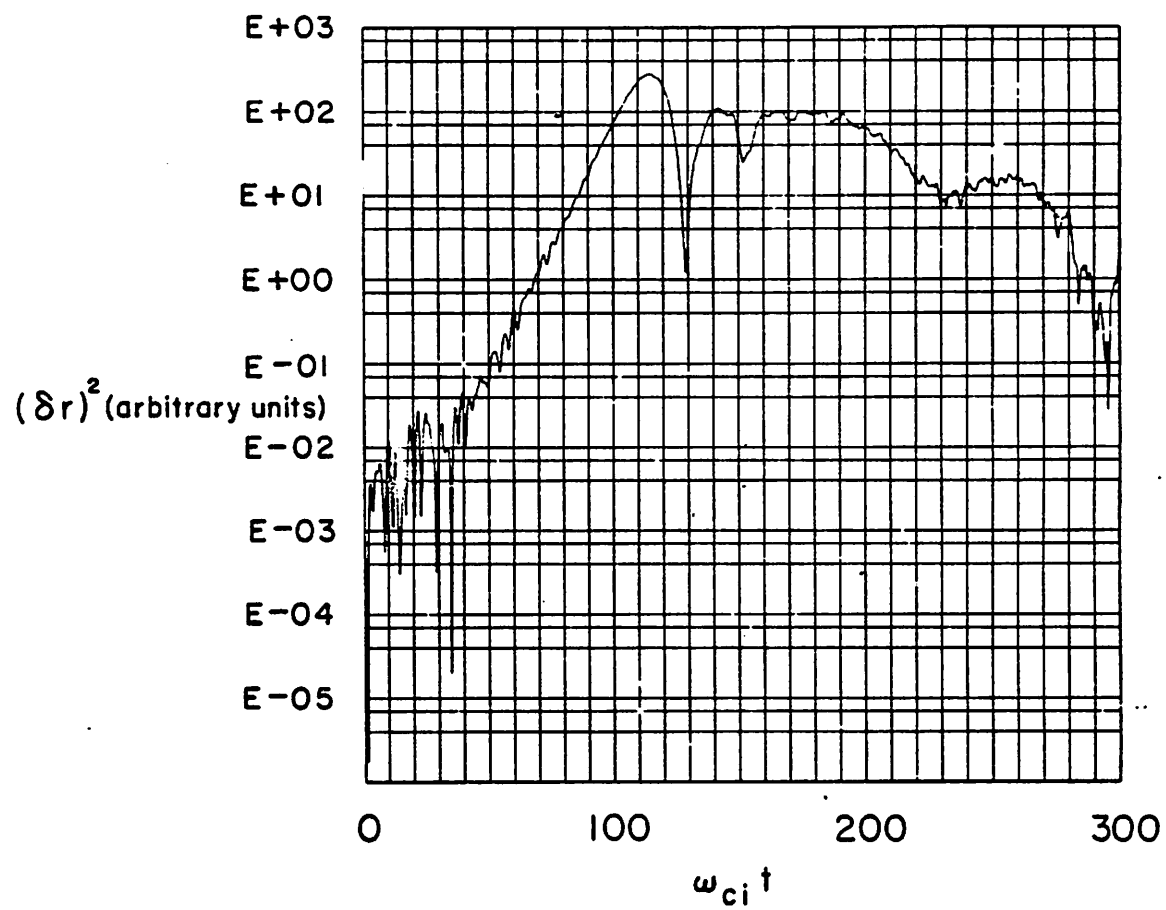


FIG. A7 $(\delta r)^2$ as a function of time for the $m=4$ mode.

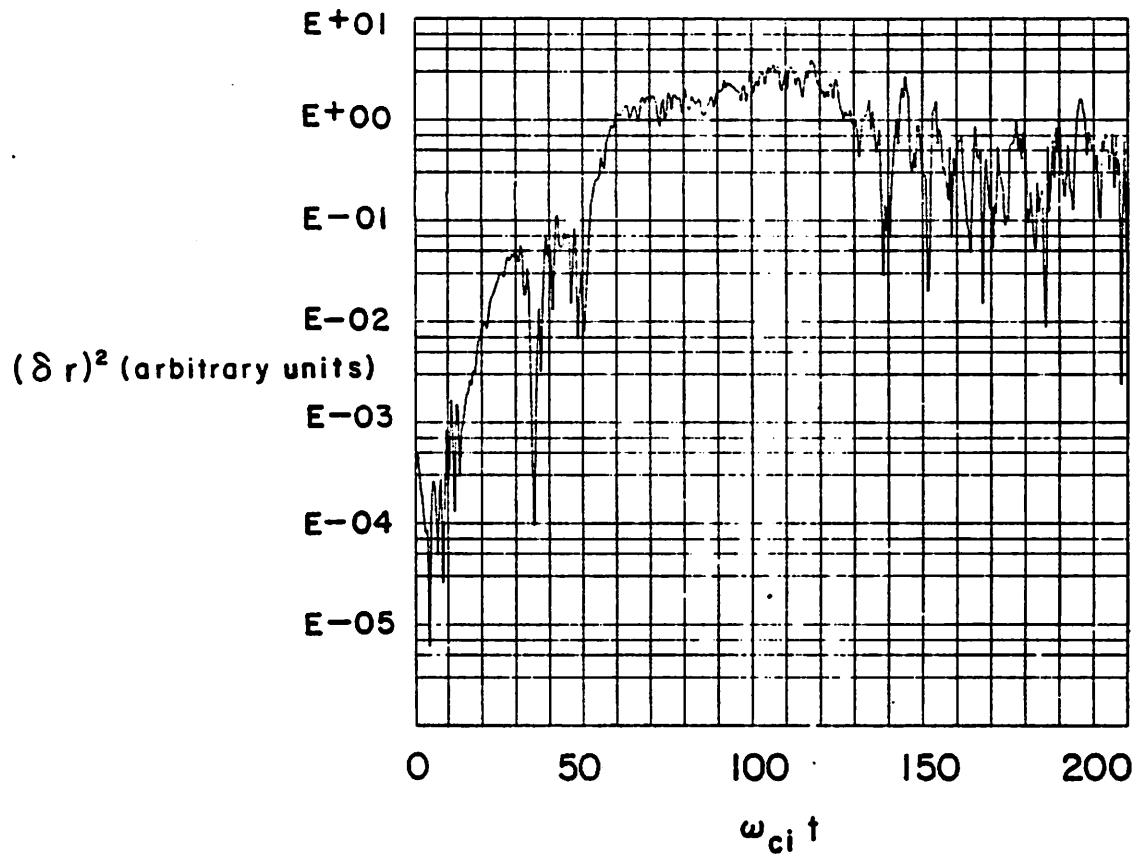


FIG. A8 $(\delta r)^2$ as a function of time for the $m=5$ mode.

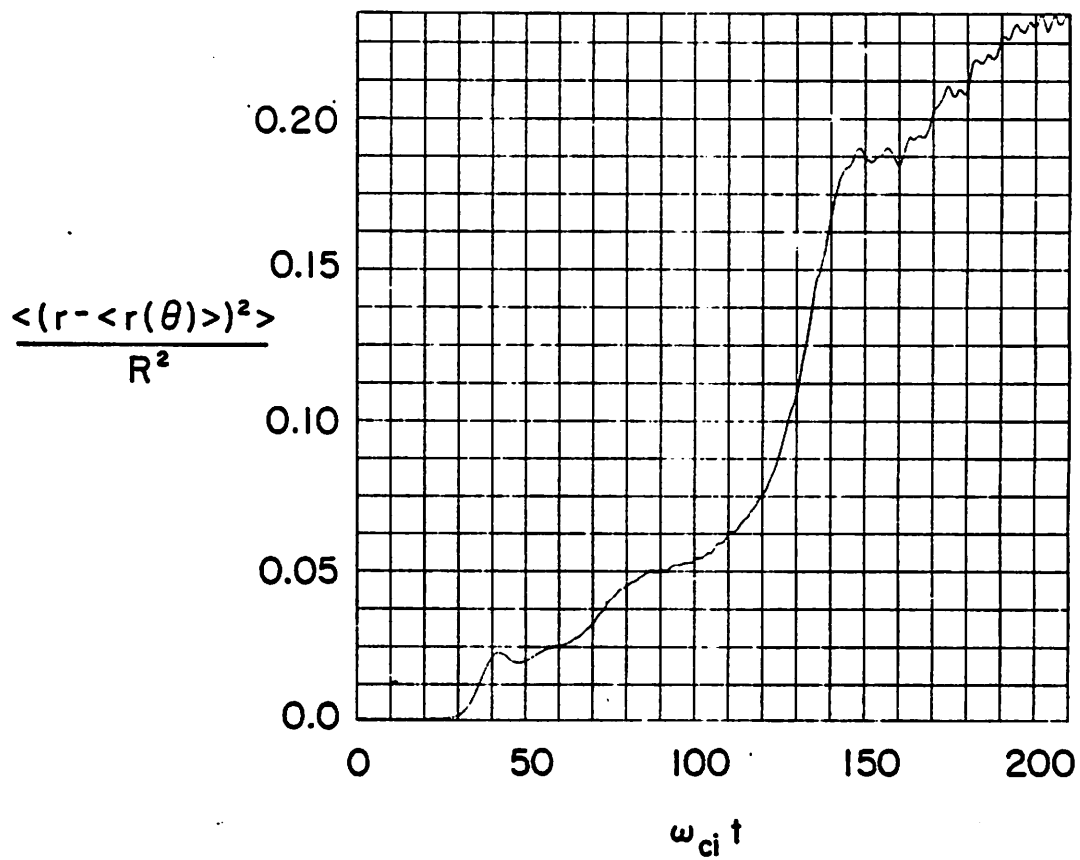


FIG. A9 $\langle (r - \langle r(\theta) \rangle)^2 \rangle$ as a function of time.

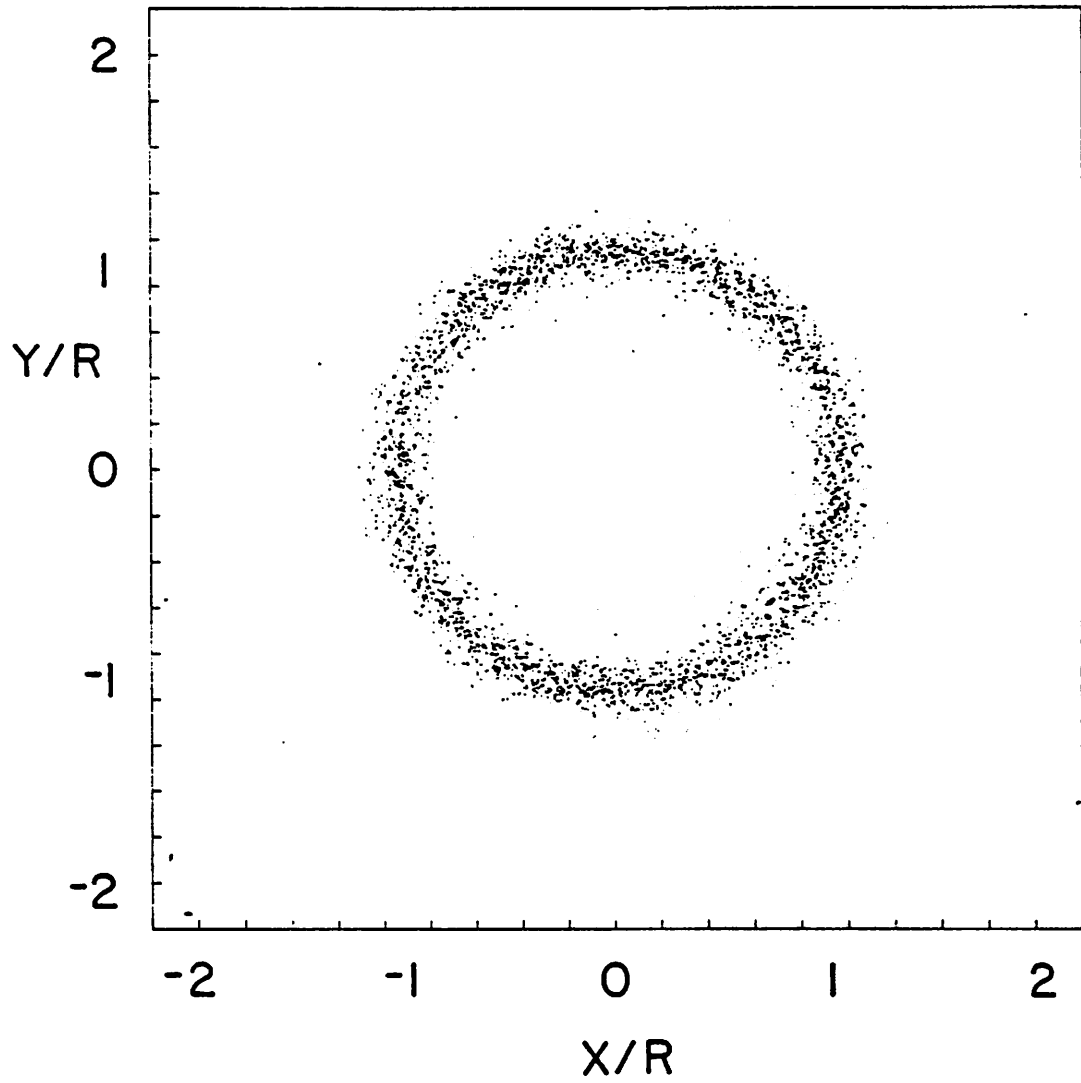


FIG. A10 Initial particle positions for layer with increased field-reversal, $\zeta=1.38$,
 $(R/a)=5$.

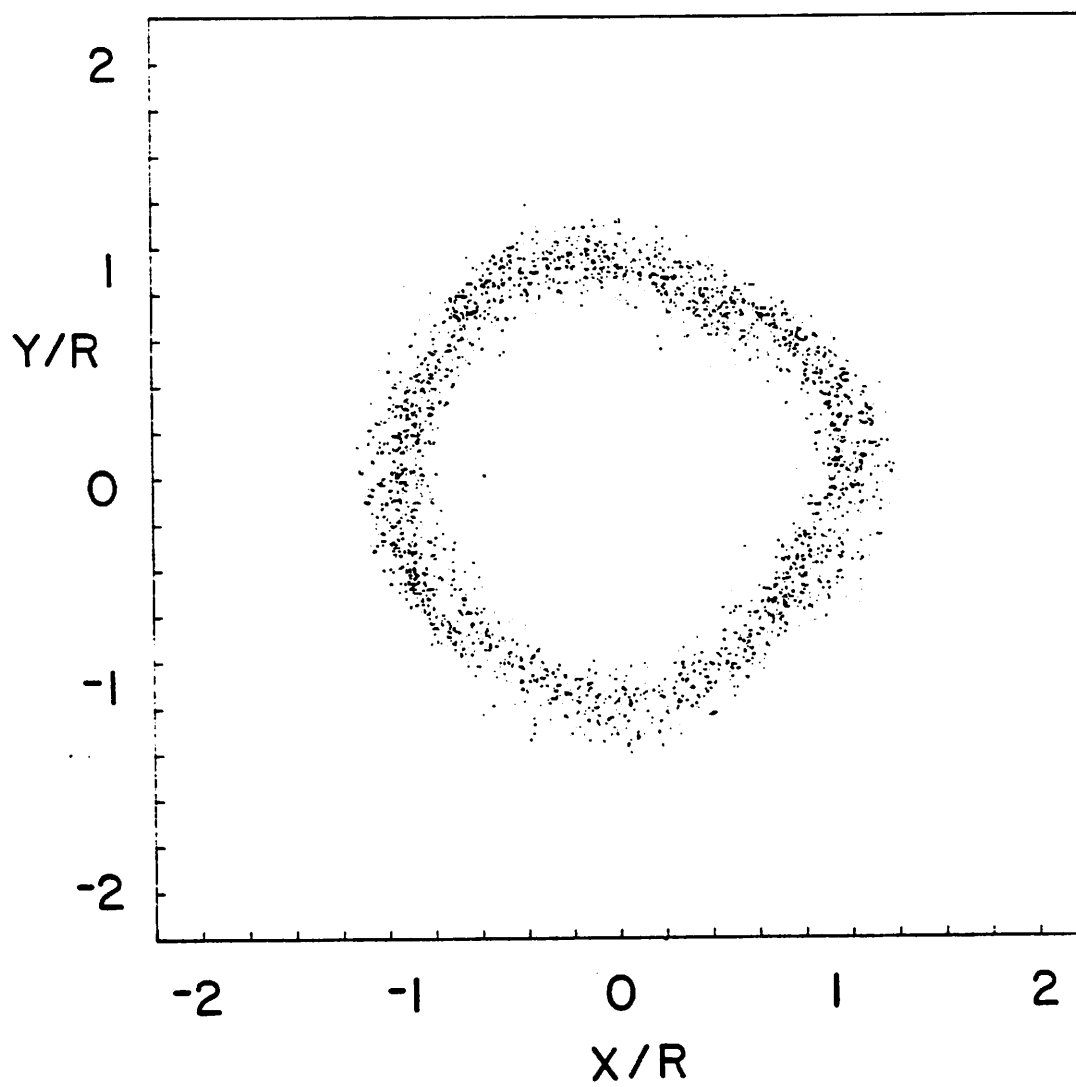


FIG. A11 Particle positions at $t=50\omega_{ci}^{-1}$. An $m=4$ mode has grown to large amplitude.

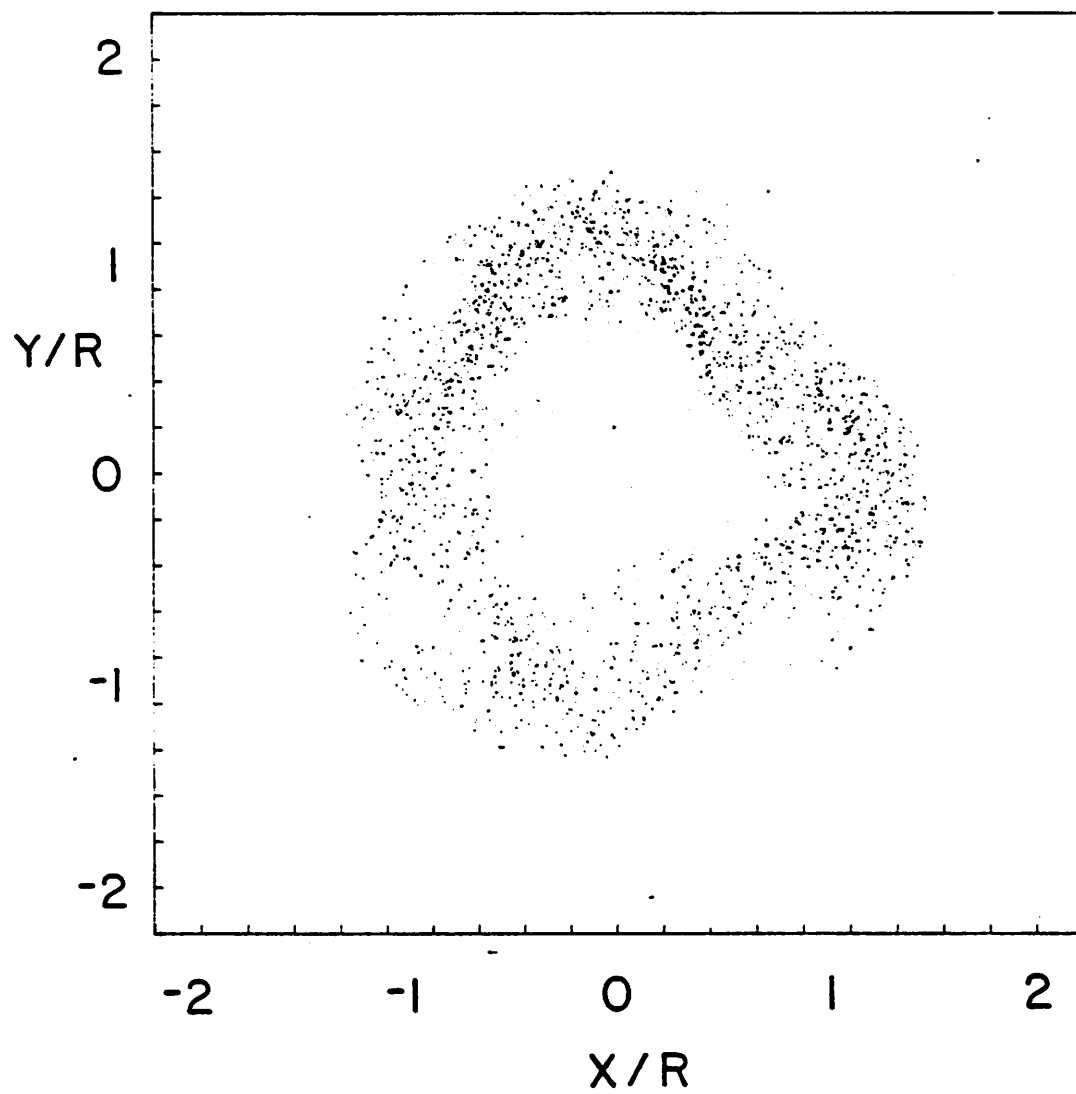


FIG.A12 Particle positions at $t=70\omega_{ci}^{-1}$. An $m=3$ mode now dominates.

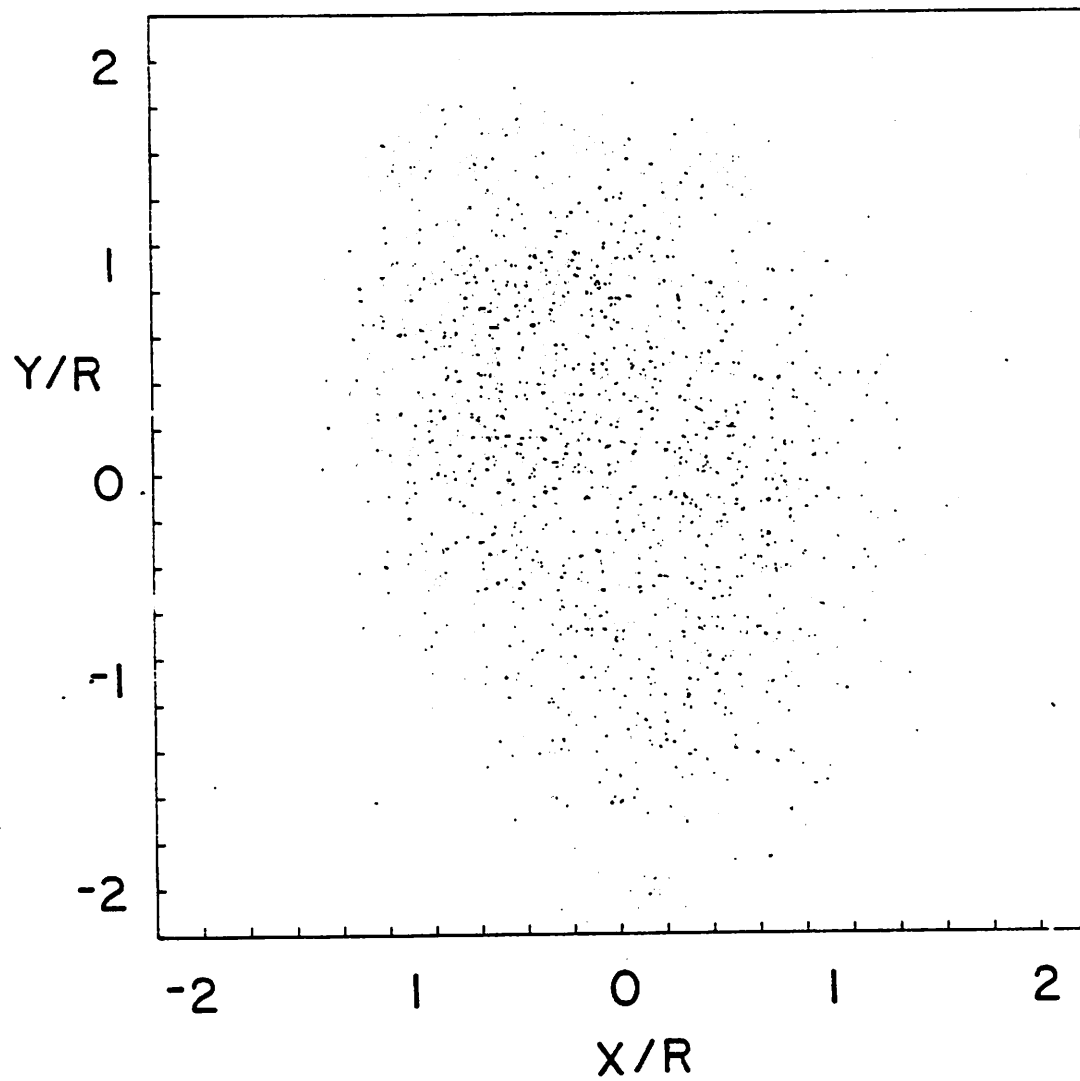


FIG.A13 Particle positions at $t=220\omega_{ci}^{-1}$. The structure of the $m=2$ mode, the last mode to saturate, is still apparent.

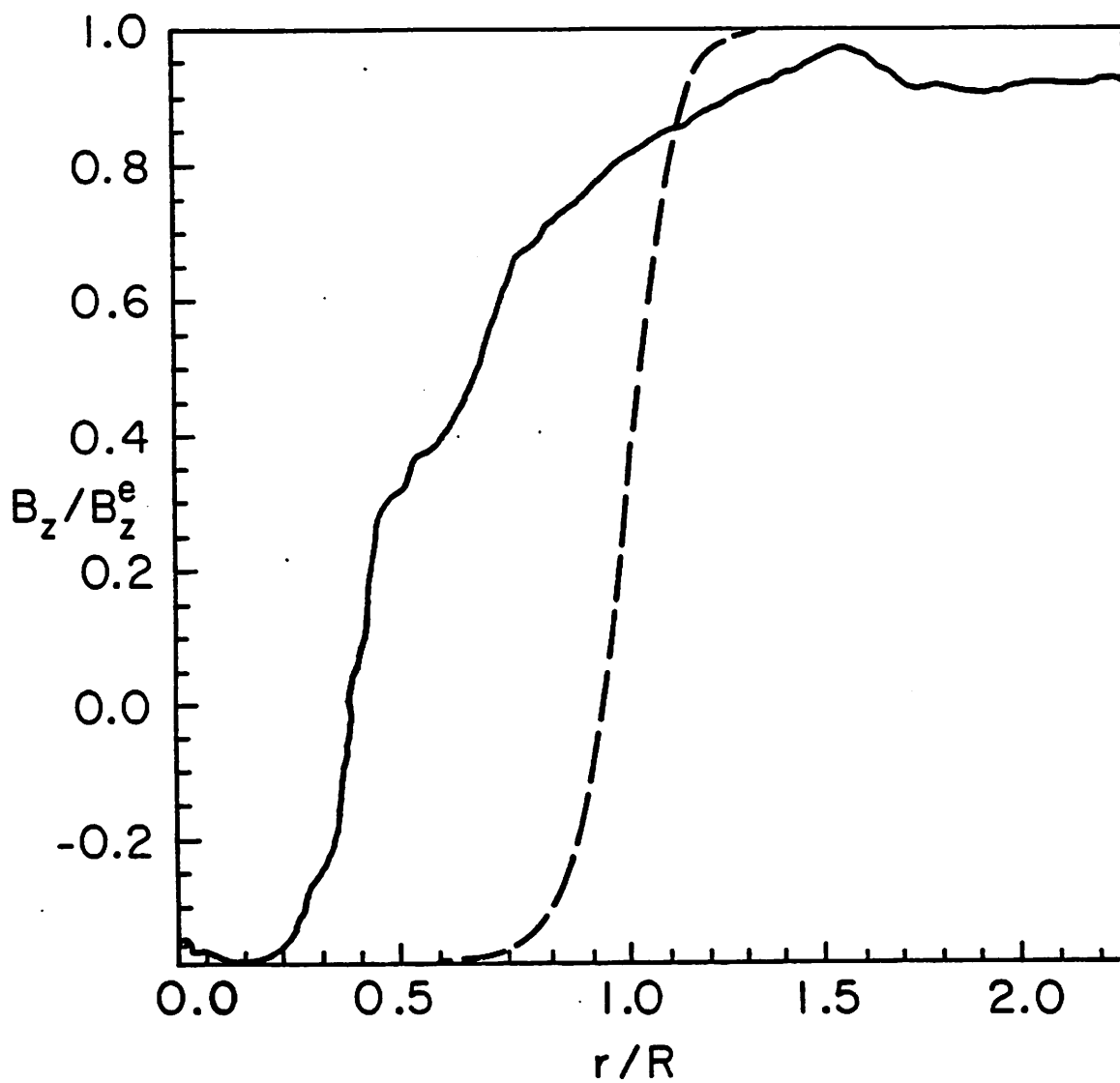


FIG. A14 Magnetic field profiles, $B_z(r)$ averaged over θ , at $t=0$ (dotted line) and at $t=220\omega_{ci}^{-1}$ (solid line).